Four-Component Relativistic DFT Calculations of EPR *g*- and Hyperfine-Coupling Tensors Using Hybrid Functionals: Validation on Transition-Metal Complexes with Large Tensor Anisotropies and Higher-Order Spin-Orbit Effects

Sebastian Gohr,[a] Peter Hrobárik,[a,*] Michal Repiský,[b] Stanislav Komorovský,[b] Kenneth Ruud,[b] Martin Kaupp[a,*]

[a] Technische Universität Berlin, Institut für Chemie, Theoretische Chemie/Quantenchemie, Sekr. C7, Straße des 17. Juni 135, 10623 Berlin, Germany; [b] Department of Chemistry, Centre for Theoretical and Computational Chemistry (CTCC), UiT The Arctic University of Norway, 9037 Tromsø, Norway

E-mail: peter.hrobarik@tu-berlin.de; martin.kaupp@tu-berlin.de

ABSTRACT: The four-component matrix Dirac-Kohn-Sham (mDKS) implementation of EPR **g**- and hyperfine **A**-tensor calculations within a restricted kinetic balance framework in the ReSpect code has been extended to hybrid functionals. The methodology is validated for an extended set of small $4d^1$ and $5d^1$ $[MEX_n]^q$ systems, and for a series of larger Ir(II) and Pt(III) d^7 complexes (S=1/2) with particularly large **g**-tensor anisotropies. Different density functionals (PBE, BP86, B3LYP-*x*HF, PBE0-*x*HF) with variable exact-exchange admixture *x* (ranging from 0% to 50%) have been evaluated, and the influence of structure and basis set has been examined. Notably, hybrid functionals with exact-exchange admixture of about 40% provide the best agreement with experiment and clearly outperform the generalized-gradient approximation (GGA) functionals, in particular for the hyperfine couplings. Comparison with computations at the one-component second-order perturbational level within the Douglas-Kroll-Hess framework (1c-DKH), and a scaling of the speed of light at the four-component mDKS level, provide insight into the importance of higher-order relativistic effects for both properties. In the more extreme cases of some iridium(II) and platinum(III) complexes, the widely used leading-order perturbational treatment of SO effects in EPR calculations fails to reproduce not only the magnitude but also the sign of certain g-shift components (with the contribution of higher-order SO effects amounting to several hundreds of ppt in 5d complexes). The four-component hybrid mDKS calculations perform very well, giving overall good agreement with the experimental data.

Keywords. Dirac-Kohn-Sham calculations, Dirac-Coulomb Hamiltonian, exchange-correlation functionals, **g**-tensor, hyperfine tensor, relativistic effects, spin-orbit coupling.

Introduction

Electron paramagnetic resonance (EPR) spectroscopy[1-4] of open-shell transition-metal complexes is an important spectroscopic tool in a variety of research fields, ranging from a mapping of defects in solid-state materials and surfaces (e.g. in heterogeneous catalysis)[5,6] via studies of single-molecule magnets[7-10] to those of paramagnetic metalloenzyme sites.[11-13] Use of quantum-chemical methods to aid the evaluation and interpretation of EPR parameters, or to elucidate the structure of new, sometimes exotic, species based on EPR experiments has seen tremendous developments over the past 20 years.[4,14-17] Calculations of molecular properties such as the electronic **g**-tensor and hyperfine coupling (HFC) **A**-tensors are, however, still a considerable challenge for quantum-chemical methods due to the large sensitivity of these intrinsic parameters to the molecular structure as well as to relativistic and environmental effects.[4] Due to the spin-orbit-dominated nature of **g**-tensors and the dependence of HFCs on spin-density distributions near the nuclei, spin-orbit (SO) and scalar relativistic effects range from important to crucial in this context, and they grow towards the lower regions of the Periodic Table. Subtle electron exchange and correlation effects are furthermore relevant, in particular for isotropic HFCs. Accurate and efficient relativistic electronic-structure methods are thus mandatory in order to provide useful quantum-chemical tools for reliable predictions and interpretations of non-trivial EPR spectra.

Multi-reference *ab initio* methods at the Douglas-Kroll-Hess (DKH) relativistic level have been promoted for calculations of **g**-tensors and zero-field splittings,[18-20] but currently they are feasible only for small systems of around 15 atoms.[21] Similar limitations apply to restricted active space state interaction (RASSI)-based calculations of HFCs.[22] Recent density matrix renormalization group (DMRG) calculations of hyperfine couplings[23] have so far also been limited to small molecules, and to scalar relativistic levels.[24] Coupled-cluster and configuration-interaction calculations of **g**-tensors[25-26] and relativistic coupled-cluster calculations of HFC tensors[27] suffer from the same limitations. While such approaches may in

the future become more important for EPR parameter calculations, computations for larger systems, for example the transition metal complexes we focus on in this work, will have to rely on density functional theory (DFT) methods for some time to come. Initial DFT implementations of **g**-tensors and HFCs either included SO effects by leading-order perturbation theory[28-34] or variationally in two-component quasirelativistic spin-restricted zero-order regular approximation (ZORA) or Douglas-Kroll-Hess calculations.[35-38] Subsequently, the Kramers-unrestricted two-component DKH,[39-40] resolution of identity Dirac-Kohn-Sham (DKS-RI) method[41] and, more recently, four-component DFT calculations of EPR parameters became available, allowing both spin polarization and higher-order SO effects to be included simultaneously.[42-43] The advantage of fully relativistic approaches is not only the variational treatment of SO effects, but also that they avoid the additional operator transformations associated with picture-change effects in two-component frameworks (such as the DKH method).[44-47]

Our initial assessment of the four-component matrix Dirac-Kohn-Sham (mDKS) method for smaller heavy-atom radicals and for medium-sized molybdenum(V) and tungsten(V) complexes has revealed the advantages of this method.[48] The initial mDKS implementation of EPR parameters in the ReSpect program was, however, restricted to generalized-gradient approximation (GGA)-type functionals. As admixture of exact exchange (EXX) is known to be beneficial for both **g**-tensors,[30,49-50] and in particular for isotropic hyperfine coupling constants[51-53] of transition-metal complexes, the use of global hybrid functionals is desirable also in a 4-component framework. Here we thus extend the implementation and validation of the four-component mDKS method to hybrid functionals. Moreover, metal HFCs for 4d and 5d transition-metal complexes will be evaluated more systematically than done in the past. Evaluating and benchmarking the optimal EXX admixture in hybrid functionals will initially be done for a larger set of previously studied small $4d^1$ and $5d^1$ transition-metal complexes $[M(E)X_4]^q$ and $[M(E)X_5]^q$ (M = Mo, Tc, W, Re, Os; E = O, N; X = F, Cl, Br; q = 0, -1, -2)

with an extensive set of experimental data. Similar systems have also been in the focus of two-component ZORA studies,[54-55] but without a comparably systematic evaluation of the optimal EXX admixture in global hybrids. An extension to the fully relativistic four-component level is in any case desirable. We use this test set to derive a "best functional" to be suggested as part of a fully relativistic computational protocol for applications to a wider variety of 4d and 5d systems. This approach is then applied and tested for a selection of larger Ir(II) and Pt(III) d^7 complexes exhibiting particularly large **g**-tensor anisotropies. By comparison with scalar relativistic DKH calculations with leading-order perturbation treatment of spin-orbit effects, we will demonstrate the importance of higher-order SO effects and show that in some cases these effects are necessary in order to even reproduce qualitative features (such as the sign of certain tensor components).

Theory

Relativistic calculations of EPR parameters have a long history.[2, 4,56] Here, we focus mostly on the theoretical foundations of the relativistic matrix Dirac-Kohn-Sham (mDKS) method as implemented in the ReSpect program package,[57] involving a restricted kinetically balanced basis set for the small component of the wave function.[58-59] Consistent with ref. 42, in the following we use the Hartree system of atomic units. i denotes occupied positive energy orbitals, while λ, τ are basis-function indices, and u, v the cartesian directions. c is the speed of light, and summation over repeated indices is assumed. $0_{2\times2}$ and $1_{4\times4}$ are the two-by-two zero matrix and the four-by-four unit matrix, respectively.

To derive working equations for the EPR parameters, we start with the conventional form of the free-particle Dirac equation,

$$[\boldsymbol{\beta}c^2 + c(\boldsymbol{\alpha}\cdot\boldsymbol{p})]\varphi_i = E_i\varphi_i, \qquad (1)$$

where φ_i is the 4-spinor wavefunction, separable into two 2-spinor parts, denoted as large (L) and small (S) components

$$\varphi_i = \begin{pmatrix} \varphi_i^L \\ \varphi_i^S \end{pmatrix}. \qquad (2)$$

α and β denote the 4×4 Dirac matrices

$$\boldsymbol{\alpha} = \begin{bmatrix} 0_{2\times2} & \boldsymbol{\sigma} \\ \boldsymbol{\sigma} & 0_{2\times2} \end{bmatrix} \qquad \boldsymbol{\beta} = \begin{bmatrix} 1_{2\times2} & 0_{2\times2} \\ 0_{2\times2} & -1_{2\times2} \end{bmatrix} \qquad (3)$$

and $\boldsymbol{\sigma}$ refers to the 2×2 Pauli spin matrices

$$\sigma_x = \begin{bmatrix} 0 & 1 \\ 1 & 0 \end{bmatrix} \quad \sigma_y = \begin{bmatrix} 0 & -i \\ i & 0 \end{bmatrix} \quad \sigma_z = \begin{bmatrix} 1 & 0 \\ 0 & -1 \end{bmatrix}. \qquad (4)$$

Using the minimal electromagnetic coupling for the electron

$$\boldsymbol{p} \to \boldsymbol{\pi} = \boldsymbol{p} + \tfrac{1}{c}\boldsymbol{A} \qquad E \to E - V, \qquad (5)$$

together with an energy alignment to the non-relativistic energy scale ($\boldsymbol{\beta}' = \boldsymbol{\beta} - 1_{4\times4}$), gives the Dirac equation for an electron in the presence of an electromagnetic field

$$h_{\mathrm{D}}\varphi_i = E_i\varphi_i,$$

$$h_{\mathrm{D}} = \boldsymbol{\beta}' c^2 + c(\boldsymbol{\alpha}\cdot\boldsymbol{\pi}) + V_{4\times4} = \begin{bmatrix} 0_{2\times2} & c(\boldsymbol{\sigma}\cdot\boldsymbol{\pi}) \\ c(\boldsymbol{\sigma}\cdot\boldsymbol{\pi}) & -2c^2 \end{bmatrix} + V_{4\times4}\ . \qquad (6)$$

The vector potential $\boldsymbol{A}$ has two contributions: one from an external uniform magnetic field $\boldsymbol{B}$ and one from the nuclear magnetic moment $\boldsymbol{\mu}^M$ of nucleus M

$$\boldsymbol{A} = \boldsymbol{A}_{\boldsymbol{B}} + \boldsymbol{A}_{\boldsymbol{\mu}^M}$$

$$\boldsymbol{A}_{\boldsymbol{B}} = \frac{1}{2}(\boldsymbol{B}\times\boldsymbol{r}_G) \qquad \boldsymbol{r}_G = \boldsymbol{r} - \boldsymbol{r}_0 \qquad (7)$$

$$\boldsymbol{A}_{\boldsymbol{\mu}^M} = \frac{\boldsymbol{\mu}^M \times \boldsymbol{r}_M}{r_M^3} \qquad \boldsymbol{r}_M = \boldsymbol{r} - \boldsymbol{R}_M$$

where $\boldsymbol{r}_0$ corresponds to an arbitrary fixed gauge origin, and $\boldsymbol{R}_M$ is the position of nucleus M. Note that $\boldsymbol{A}_{\boldsymbol{\mu}^M}$ in eq. (7) is given for a point nucleus magnetic moment, whereas the formulation of a finite nuclear magnetic moment entails a complicated expression, see for instance ref. 43. The connection between $\boldsymbol{\mu}^M$ and the nuclear spin $\boldsymbol{I}^M$ is given by the gyromagnetic ratio γ^M: $\boldsymbol{\mu}^M = \gamma^M \boldsymbol{I}^M$.

Within the Kohn-Sham density functional theory, the scalar potential $V_{4\times4}$ contains the electron-nucleus Coulomb potential V_{nuc}, the electron-electron interaction V_{ee}, as well as the Kohn-Sham exchange-correlation potential V_{xc}, whose implementation involves a "non-collinear" formalism.[60] For the calculation of the exchange-correlation potential, the usual non-relativistic functionals are employed, though they will depend on relativistic density and spin densities. From here on we will use a superscript "(J_v)" to indicate the dependence of the electronic energy on the orientation of the total magnetization vector $\boldsymbol{J}$ along the v axis.

Hence,

$$
\begin{aligned}
V^{(J_v)} &= V_{\mathrm{nuc}} + V_{\mathrm{ee}}^{(J_v)} + V_{\mathrm{xc}}^{(J_v)}, \\
V_{\mathrm{nuc}} &= -\sum_M \frac{Z_M}{r_M} 1_{4\times4}, \\
V_{\mathrm{xc}}^{(J_v)} &= \begin{bmatrix} v_{2\times2}^{xc}\left[1-\xi, \rho_k^{(J_v)}\right] & 0_{2\times2} \\ 0_{2\times2} & v_{2\times2}^{xc}\left[1-\xi, \rho_k^{(J_v)}\right] \end{bmatrix}.
\end{aligned}
\qquad (8)
$$

Here, ρ_k (where $k = 0, x, y, z$) describes the relativistic electron density (ρ_0) and the three spin densities (ρ_x, ρ_y, ρ_z), whereas $v_{2\times2}^{xc}\left[1-\xi, \rho_k^{(J_v)}\right]$ describes the noncollinear exchange-correlation potential,

$$
\rho_k^{(J_v)} = {\varphi_i^{(J_v)}}^{\dagger} \mathcal{M}_k \varphi_i^{(J_v)}, \qquad \mathcal{M}_0 = 1_{4\times4}, \qquad \mathcal{M}_{k\neq0} = \begin{pmatrix} \sigma_k & 0_{2\times2} \\ 0_{2\times2} & \sigma_k \end{pmatrix}. \qquad (9)
$$

Note, that V_{nuc} in eq. (8) is given for a point charge distribution model of nucleus, whereas a more realistic description of the nuclear structure requires a finite-size distribution model, as described *e.g.* in ref. 43.

The electron-electron term V_{ee}, has the form

$$
V_{\mathrm{ee}}^{(J_v)} = \int \frac{\rho_0^{(J_v)}(\boldsymbol{r}')}{|\boldsymbol{r}-\boldsymbol{r}'|}\, \mathrm{dV}'\, 1_{4\times4} - \xi K_{4\times4}^{(J_v)}, \qquad (10)
$$

$$
K_{4\times4}^{(J_v)}\, \varphi_i^{(J_v)}(\boldsymbol{r}) = \left[\int \frac{\varphi_j^{\dagger(J_v)}(\boldsymbol{r}')\, \varphi_i^{(J_v)}(\boldsymbol{r}')}{|\boldsymbol{r}-\boldsymbol{r}'|}\, \mathrm{dV}'\right] \varphi_j^{(J_v)}(\boldsymbol{r}), \qquad (11)
$$

and consists of the classical Coulomb interaction and the exact-exchange interaction $\left(K_{4\times4}^{(J_v)}\right)$. The scalar coefficient ξ weights the admixture of the exact-exchange contribution with the DFT exchange-correlation part $\left(V_{\mathrm{xc}}^{(J_v)}\right)$, that gives rise to pure Dirac Hartree-Fock ($\xi = 1$), pure DKS ($\xi = 0$), or hybrid schemes ($0 < \xi < 1$).

Our approach uses restricted kinetically balanced (RKB) basis sets for the small components:

$$
\begin{aligned}
\varphi_i^{\mathrm{L}(J_v)} &= \boldsymbol{C}_{\lambda i}^{\mathrm{L}(J_v)} \chi_\lambda, \\
\varphi_i^{\mathrm{S}(J_v)} &= \boldsymbol{C}_{\lambda i}^{\mathrm{S}(J_v)} \frac{1}{2c} \boldsymbol{\sigma}\cdot\boldsymbol{p} \chi_\lambda,
\end{aligned}
\qquad (12)
$$

with χ_λ being the λth Gaussian basis function and $\boldsymbol{C}$ the expansion coefficients.

The **g**-tensor can be calculated following the approach of refs. [39,42] as

$$g_{uv} = \frac{2c}{\langle \tilde{S}_v \rangle} \frac{\mathrm{d}E(J_v, \boldsymbol{B})}{\mathrm{d}B_u}\bigg|_{\boldsymbol{B}=0} \qquad (13)$$

where $\langle \tilde{S}_v \rangle$ is an effective spin of the molecule and J_v is the magnetization (both along the v direction). To use this ansatz, it is necessary to properly choose the three directions ($v = x, y, z$) of J_v as described in refs. 39,40 and to perform three separate energy calculations. Similarly, the hyperfine coupling tensor of atom M can be defined as[43]

$$A_{uv}^{M} = \frac{1}{\langle \tilde{S}_v \rangle} \frac{\mathrm{d}E(J_v, \boldsymbol{I}^M)}{\mathrm{d}I_u^M}\bigg|_{\boldsymbol{I}^M=0} \qquad (14)$$

where $\boldsymbol{I}^M$ represents the nuclear spin of atom M.

Applying the Hellmann-Feynman theorem to eqs. (13) and (14), with molecular orbitals expanded according to eq. (12), gives the final expressions for the **g**-tensor

$$g_{uv} = \frac{1}{\langle \tilde{S}_v \rangle} \mathrm{Tr}\left[\begin{pmatrix} 0_{2\times2} & {\boldsymbol{\Lambda}_{B_u}}^{\dagger} \\ \boldsymbol{\Lambda}_{B_u} & 0_{2\times2} \end{pmatrix} \begin{pmatrix} \boldsymbol{P}^{\mathrm{LL}(J_v)} & \boldsymbol{P}^{\mathrm{LS}(J_v)} \\ \boldsymbol{P}^{\mathrm{SL}(J_v)} & \boldsymbol{P}^{\mathrm{SS}(J_v)} \end{pmatrix} \right], \qquad (15)$$

where

$$\left(\Lambda_{B_u}\right)_{\lambda\tau} = \frac{1}{2} \langle \chi_\lambda | \boldsymbol{\sigma} \cdot \boldsymbol{p} (\boldsymbol{r}_G \times \boldsymbol{\sigma})_u | \chi_\tau \rangle, \qquad (16)$$

$$\begin{pmatrix} \boldsymbol{P}^{\mathrm{LL}(J_v)} & \boldsymbol{P}^{\mathrm{LS}(J_v)} \\ \boldsymbol{P}^{\mathrm{SL}(J_v)} & \boldsymbol{P}^{\mathrm{SS}(J_v)} \end{pmatrix} = \sum_{i}^{occ} \begin{pmatrix} \boldsymbol{C}_{(i)}^{\mathrm{L}(J_v)} \\ \boldsymbol{C}_{(i)}^{\mathrm{S}(J_v)} \end{pmatrix} \begin{pmatrix} \boldsymbol{C}_{(i)}^{\mathrm{L}(J_v)\dagger} & \boldsymbol{C}_{(i)}^{\mathrm{S}(J_v)\dagger} \end{pmatrix}, \qquad (17)$$

and the HFC-tensor

$$A_{uv}^{M} = \frac{1}{2c\langle \tilde{S}_v \rangle} \mathrm{Tr}\left[\begin{pmatrix} 0_{2\times2} & {\boldsymbol{\Gamma}_{I_u^M}}^{\dagger} \\ \boldsymbol{\Gamma}_{I_u^M} & 0_{2\times2} \end{pmatrix} \begin{pmatrix} \boldsymbol{P}^{\mathrm{LL}(J_v)} & \boldsymbol{P}^{\mathrm{LS}(J_v)} \\ \boldsymbol{P}^{\mathrm{SL}(J_v)} & \boldsymbol{P}^{\mathrm{SS}(J_v)} \end{pmatrix} \right], \qquad (18)$$

with

$$\left(\Gamma_{I_u^M}\right)_{\lambda\tau} = \gamma^M \left\langle \chi_\lambda \middle| \boldsymbol{\sigma} \cdot \boldsymbol{p} \left(\frac{\boldsymbol{r}_M \times \boldsymbol{\sigma}}{r_M^3} \right)_u \middle| \chi_\tau \right\rangle. \qquad (19)$$

Note again that $\left(\Gamma_{B_u}\right)_{\lambda\tau}$ will differ for a finite-nucleus magnetic moment, as shown in ref. 43.

The noncollinear Kramers-unrestricted calculations require several SCF calculations with different orientations of the magnetization vecor ***J*** to obtain the entire tensor information (see above). Jayatilaka[61] suggested that six calculations are needed if the principal axes are not known. *A priori* knowledge of the proper orientation reduces this to three calculations with orthogonal orientations, where the J_v directions coincide with the principal axes of the **g**-tensor or HFC **A**-tensors, respectively.

We finally note that our four-component implementation is derived from the Dirac-Coulomb Hamiltonian. It therefore neglects the spin-other-orbit (SOO) terms arising from the Breit Hamiltonian, but in contrast to some early two-component DFT implementations using the "effective potential approach", exchange contributions to the spin-same-orbit term[62] are properly accounted for. The SOO contributions are of lesser relative importance compared to the other SO terms for heavier systems, on which this work focusses.[48] Below, we will estimate the importance of the neglected SOO terms based on a perturbational treatment of SO effects.

Computational Details

Structures. Structures of the small d^1 transition metal benchmark systems were optimized with GAUSSIAN 09[63] using the PBE0[64-65] hybrid functional. Quasirelativistic energy-consistent small-core pseudopotentials (effective-core potentials, ECP)[66] were used for the metal centers, with (7s7p5d1f)/[6s4p3d1f] and (8s7p6d1f)/[6s4p3d1f] Gaussian-type orbital valence basis sets for the 4d and 5d metal atoms, respectively. Ligand atoms were treated with an all-electron def2-TZVP basis set.[67] If not stated otherwise, for calculations of the large iridium and platinum complexes, the experimentally determined structures have been used. These have been taken from the same references as the EPR data (cf. Table 2 and references therein). Due to the absence of an experimental structure for $[Pt(C_6Cl_5)_4]^-$, this complex has been optimized at the PBE0-D3(BJ)/def2-TZVP/ECP level, including Grimme's atom-

pairwise D3 dispersion corrections[68] with Becke-Johnson (BJ) damping.[69] To assess the influence of input structures on quality of computed EPR parameters, we also optimized structures of some larger Ir(II) and Pt(III) complexes, for which X-ray structure data are known, at the same computational level and compared computed spectroscopic parameters (cf. Table S12 in Supporting Information).

EPR Parameters Calculations. All property calculations at the one-component relativistic level were done in the older ReSpect-MAG program.[70] Here, single-point self-consistent field (SCF) calculations using tight convergence criteria (energy and density matrix convergence 10^{-6} and 10^{-8} a.u., respectively) and an ultrafine integration grid (99 radial shells and 590 angular points per shell), along with Douglas-Kroll-Hess second-order corrections (DKH2) to account for scalar relativity, were done with the GAUSSIAN code,[63] using a Gaussian-type finite nuclear-charge model. Subsequently, the unrestricted Kohn-Sham orbitals were transferred by interface routines to the ReSpect-MAG property package (invoking a "fine" grid with 64 radial grid points), which was then used to carry out the **g**-tensor calculations at the second-order perturbational level of theory. Spin-orbit (SO) effects in these calculations were included using the atomic mean-field approximation (AMFI)[71] at the first-order DKH level, neglecting picture-change effects for the orbital-Zeeman term (this is expected to be a reasonable approximation,[47] and in any case sufficient for the intended comparison; see also Table S10 in Supporting Information). Additionally, scalar relativistic HFC calculations at DKH2 level also used the orbitals transferred from GAUSSIAN and applied the DKH2-transformed HFC operators reported in ref. 44, with a Gaussian finite-nucleus magnetic moment.[72] In this work, we used and evaluated several basis set combinations. Dyall basis sets[73-76] of double-zeta (DZ), valence double-zeta (VDZ) and triple-zeta (TZ) quality and basis sets by Hirao[77] were employed for the 4d and 5d metal centers. Fully uncontracted Huzinaga-Kutzelnigg-type IGLO-II and IGLO-III basis sets[78] were used for the light ligand atoms ($Z < 18$).

The 4c-mDKS calculations were carried out completely with the RESPECT program,[57] including a new four-component module. Calculations have been done either at the generalized gradient approximation (GGA) level (BP86[79-80] and PBE[64]) or using customized B3LYP-*x*HF[81-82] and PBE0-*x*HF functionals with variable exact-exchange admixture (indicated by *x*). All-electron basis sets of the same quality as used in the 1c-DKH calculations (see above) were also applied in the mDKS calculations with restricted kinetic balance used to automatically construct the small-component basis.

The following naming convention is used throughout the paper: <DFT functional>-*x*HF /<metal basis set>/<ligand basis set>. For instance, "PBE0-40HF/Dyall(TZ)/IGLO-III" denotes a property calculation using the PBE0 functional with a modified amount of Hartree-Fock exact exchange (in this case 40% instead of the 25% used in standard PBE0), along with the Dyall(TZ) basis for the metal center and IGLO-III for ligand atoms. Since there are no IGLO basis sets available for the heavier halogen atoms, we have employed Dyall(VTZ) basis sets for Br and Dyall(TZ) or Hirao basis sets for iodine (depending on the corresponding metal basis).

In the 4c-mDKS calculations, an integration grid of "ADAPTIVE" size for the Lebedev angular points was applied[83] and the following numbers of radial grid points were used for the indicated atoms: B, C, N, O, F: 60; P, Cl: 72; Br, Mo, Tc, I: 80; W, Re, Os, Ir, Pt: 96. In contrast to our previous work,[48] all calculations were performed without fitting of electron and spin densities.

The components of the **g**-tensor were obtained from three spin-unrestricted DFT self-consistent-field (SCF) procedures with orthogonal orientations of J_v. The principal axes in the small $[M(E)X_n]^q$ complexes are determined *a priori* by the C_{4v} point group symmetry. The orientations for the larger systems were obtained by preceding one-component **g**-tensor calculations. The molecules were oriented such that the *x*, *y*, and *z* coordinate axes point along the (one-component) **g**-tensor principal axes. We note in passing that in some highly

asymmetric Ir(II) complexes, the principal axes of the EPR tensors obtained at the 4c-mDKS level deviated notably from those of the input structure (cf. Figures S3 and S4 in Supporting Information). However, reorientation of these molecules according to these new principal axes and subsequent 4c-mDKS calculations did not affect the computed data by more than 10 ppt or 5 MHz for g-shift and HFC tensors, respectively (less than the effect of metal basis sets; see below). A common gauge origin (CGO) at the molecule's center of mass was used for the **g**-tensors. This has been shown previously to be a good choice.[48] Similarly to the 1c-DKH calculations described above, a Gaussian finite-size nucleus model was applied for the nuclear charge in the SCF and for the nuclear magnetic moment in the HFC property calculations.[43] We provide the principal components of the **g**-tensors as **Δg**-shifts in ppt, computed as deviation from the free-electron value (g_e = 2.002319): $\Delta g = (g - g_e).1000$.

To assess the influence of higher-order SO effects, we provide plots of computed Δ**g**-shifts and HFC tensor components against a "*c* scaling factor", equal to 1/ω. The factor ω scales the speed of light in the mDKS calculations as $\omega \cdot c$ and varies from 1 to 100, where the latter value approaches the non-relativistic limit and ω=1 corresponds to a fully relativistic treatment.[39-40, 48]

For comparative purposes, a few 1c-DKH2 calculations were also performed in the ORCA program package (version 3.0.1)[84] using identical functionals and basis sets, and the results were compared with those obtained at the 1c-DKH and 4c-mDKS levels in our ReSpect-MAG code (cf. Tables S10 and S11 in Supporting Information).

Results and Discussion

Benchmark study

It is known that judicious EXX admixture in hybrid functionals can improve both the **g**-tensors and in particular the isotropic metal HFCs of transition-metal complexes (see above).

For HFCs, the main issue is the description of the spin polarization of the metal s-type core shells (e.g. 2s and 3s orbitals for 3d centers), which is underestimated by (semi-)local functionals and enhanced by EXX admixture (unless spin contamination becomes an issue).[51-52] For **g**-tensors, the too covalent metal-ligand bonding at semi-local DFT levels is the main factor that is corrected for by EXX admixture. In the case of metal-centered spin density, the latter is underestimated at the LSDA or GGA levels. EXX admixture increases the metal spin density in such cases (this is expected to hold for all systems studied here). As the major SO contributions to the **g**-tensor often arise from metal SO coupling, more EXX admixture tends to increase the **g**-anisotropies in such cases[30,48] (heavy ligand atoms may modify the picture, and ligand-centered radicals behave in an opposite manner)[85]. Compared to earlier studies based on leading-order perturbation theory for the SO contributions, the present inclusion of higher-order SO (HOSO) contributions might diminish the optimal EXX admixture for the **g**-tensors, as the HOSO effects will enhance the **g**-anisotropies for a given EXX value. The effects on the isotropic HFCs are less obvious, as SO contributions may exhibit the same or opposite sign as compared to the Fermi-contact-type terms (with sometimes dramatic consequences).[86]

With these considerations in mind, we have used a test set of 17 small $4d^1$ and $5d^1$ complexes with known experimental EPR data (17 **g**-tensors, 14 metal HFC tensors), largely adapted from previous studies,[48,54-55,87] to carefully tune the optimal EXX admixture in four-component calculations using hybrid functionals, with particular emphasis on the very sensitive HFCs. Where possible, we have replaced experimental EPR values collected originally in the work of Ziegler and Patchkowskii[87] with those from more recent and reliable references (cf. Table 1 below). The complete set of results of this benchmark study for a large variety of functionals and basis sets, at the one-component second-order perturbation DKH (1c-DKH) and four-component mDKS (4c-mDKS) levels are collected in Tables S1–S4 in Supporting Information. Figures 1 and 2 compare graphically the average percentage

deviations of the 4c-mDKS results from experiment with a few selected functionals and basis sets, respectively (Tables S5 and S6 in Supporting Information give the average total and percentage deviations in more detail).

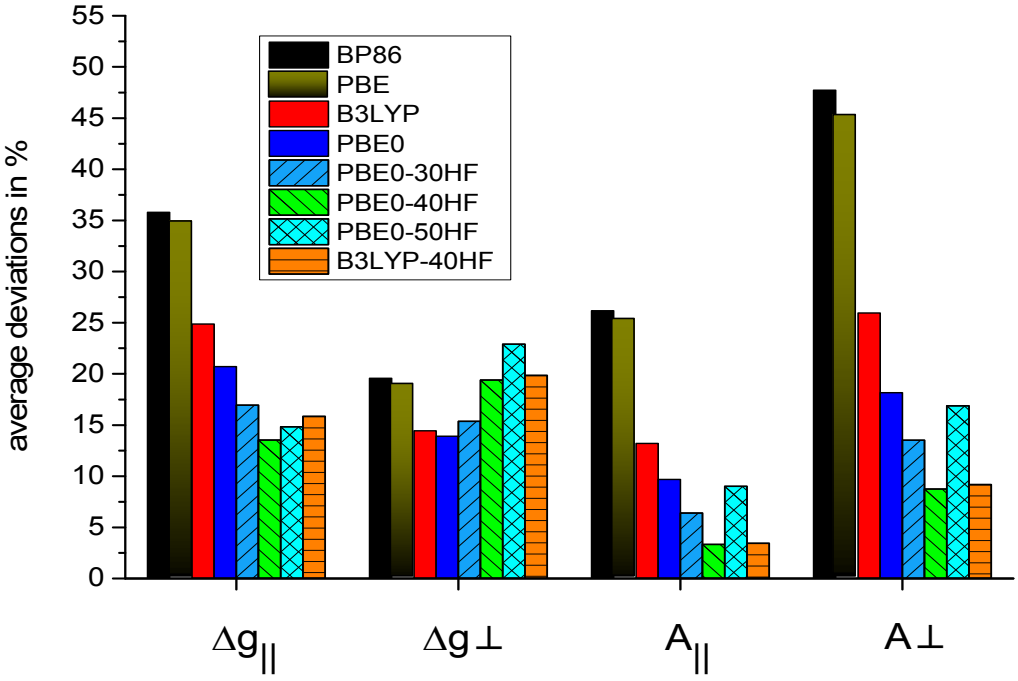

Figure 1. The effect of selected DFT functionals on the average percentage deviations of computed data from experiment for the test set of d^1 transition metal complexes (cf. Tables S1 and S6 in Supporting Information for the numerical data; Dyall(TZ)/IGLO-III basis set used). Due to their very small g-shift values (2-15 ppt), $[TcNCl_4]^-$ and $[TcNF_4]^-$ are only included in the average deviations for **A** and not for **Δg**.

Figure 1 shows clearly that pure GGA functionals, such as PBE and BP86, perform poorly for both **Δg** and **A** (with the average percentage deviations being larger than 20% for both **Δg** and **A**-tensor components), consistent with the above analyses and previous experience at one- and two-component levels.[30-31, 40, 48, 54-55] This is particularly notable for the metal HFC components (for some rhenium complexes the percentage error exceeds 60% at the GGA level; cf. $[ReNCl_4]^-$ and $[ReNBr_4]^-$ in Table S1). As expected (see above), the GGA functionals also give too small **g**-tensor anisotropies (spin densities from Natural Population

Analysis (NPA) confirm exaggerated delocalization onto the ligands at these levels; see Table S7 in Supporting Information).

Standard hybrid functionals such as B3LYP and PBE0 provide substantial improvements for both **g**- and HFC **A**-tensors (Figure 1). However, whereas deviations from the "best EXX admixtures" are small for the **g**-tensors (in fact, $\Delta g_{\perp}$ at the PBE0 level is obtained somewhat more accurately than with higher EXX values, cf. Figure 1), there is considerable room for improvement left for the HFCs. In this case, enhanced EXX admixtures reduce the average percentage deviations to below 8%. We may thus already conclude that a) the dependence of the HFCs on EXX admixture is more pronounced compared to the **g**-tensors, and b) it is easier to reach small relative errors for the HFCs. This is in part due to the fact that SO effects play a smaller relative role for the HFCs than for the **g**-tensor.[54] Moreover, the **g**-tensor is a valence property and thus more likely to be influenced by environmental effects, which we neglected here. EXX admixtures of about 30-40% appear to provide very reasonable core-shell spin polarization for the HFCs, but they also perform reasonably well for the **g**-tensors (in particular, for the $\Delta g_{\parallel}$ component). Variation of the "pure DFT ingredients" (e.g. for PBE *vs.* BP86 GGAs, or for PBE0- *vs.* B3LYP-based hybrids with the same amount of EXX) is less important than the percentage of EXX admixture alone.

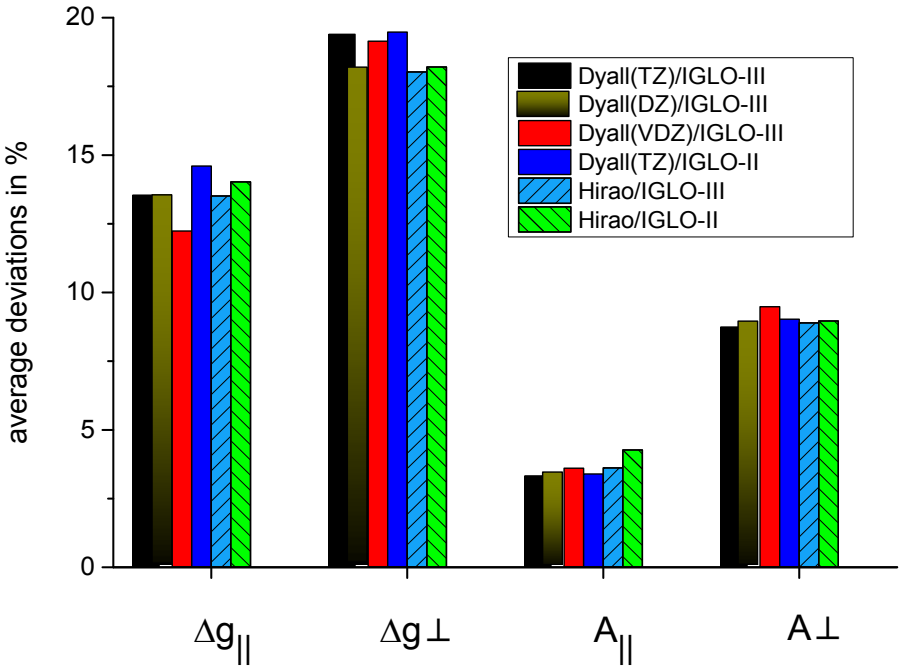

Figure 2. The effect of basis-set combinations on average percentage deviations of computed data from experiment for the test set of d^1 transition metal complexes (cf. Tables S2 and S6 in Supporting Information for numerical data; PBE0-40HF values).

Comparing the results obtained with different basis sets (see Table S2 in Supporting Information for numerical data and Figure 2 for percentage deviations for the entire set of d^1 complexes) suggests a slight preference for the Dyall(TZ)/IGLO-III combination of basis sets in case of the 4d complexes, whereas differences are small for the 5d series (except for $A_\perp$ of some rhenium complexes, where Hirao/IGLO-II performs somewhat better than Dyall(TZ)/IGLO-III, likely due to error compensation). The slightly smaller Hirao/IGLO-II basis set combination may thus be a useful alternative if computational efficiency is important (see below).

We have used perturbational 1c-DKH calculations for a few complexes to analyze the importance of the SOO term neglected in the 4c-calculations of the **g**-tensor (Table S8 in Supporting Information), as removal of the SOO term is possible for the AMFI approximation used. Adding only the separately computed one-electron and spin-same-orbit (SSO) term

provides a reference value, and we may express the SOO contributions as a percentage of that sum. Results are ~12% for the $3d^1$ complex $[CrOF_5]^{2-}$, ~4% for the $4d^1$ system $[MoOF_5]^{2-}$ and ~2% for the $5d^1$ complexes $[WOF_5]^{2-}$ and $[OsOF_5]$. Results for the 3d and 4d systems are consistent with our earlier analyses,[28] and confirm the decreasing relative role of SOO contributions as we descend the Periodic Table, and that complexes from the same row tend to exhibit very similar percentages. We thus confirm that the neglected SOO term is of minor importance compared to other inherent errors (DFT functionals, neglect of environmental and counterion effects) in the computations on the heavy-metal complexes.

We are now in a position to select a recommended computational protocol that combines 4c-mDKS calculations with a suitable functional and basis set. From Figure 1, it is clear that hybrid functionals are superior to GGA functionals for both **g**- and HFC **A**-tensors. Whereas the **g**-tensor components depend somewhat less on the EXX admixture than the HFCs, both are reasonably well reproduced by elevated values of x in the range of 30–40% (noting that we arrive at somewhat smaller percentage deviations for HFCs than for the **g**-tensors; cf. Figure 1). We find 30 to 35 % of EXX (cf. Table S1 in Supporting Information) to be somewhat better than 40% for the $4d^1$ systems and the reverse for the $5d^1$ complexes. However, the differences for the $4d^1$ complexes are too small to warrant different protocols for the two transition-metal series. Keeping also in mind the slightly larger importance of the neglected SOO contributions for the 4d systems, we recommend hybrid functionals with roughly 40% of Hartree-Fock exchange as a good compromise for the entire test set, and for both **g**- and **A**-tensors. The mDKS/PBE0-40HF/Dyall(TZ)/IGLO-III level (or its B3LYP-40HF analogue) based on good-quality structures, should thus provide excellent predictive power for the EPR parameters of 4d and 5d complexes. Results for the benchmark set at this recommended level are reported in Table 1. Further below we will investigate if this computational protocol is also accurate for rather different types of larger complexes.

Table 1. Comparison of experimental and computed electronic Δg-shift and metal HFC tensor principal components at the recommended 4c-mDKS/PBE0-40HF/Dyall(TZ)/IGLO-III level for the benchmark set of $4d^1$ and $5d^1$ complexes

		Δg_{iso} [ppt]	$\Delta g_{\parallel}$ [ppt]	$\Delta g_{\perp}$ [ppt]	A_{iso} [MHz]	$A_{\parallel}$ [MHz]	$A_{\perp}$ [MHz]	ref.	add. refs.
$[MoNCl_4]^{2-}$	calcd.	–52	–108	–24	205	293	161		
	expt.	–44	–96	–18	-	-	-	88	
$[MoOF_4]^{-}$	calcd.	–81	–104	–70	175	272	126		
	expt.	–87	–108	–77	-	268	-	89	
$[MoOCl_4]^{-}$	calcd.	–48	–26	–58	140	223	98		
	expt.	–49	–37	–56	145	227	103	89	90-91
$[MoOF_5]^{2-}$	calcd.	–110	–113	–109	183	278	135		
	expt.	–104	–128	–91	183	279	135	92	93-94
$[MoOBr_5]^{2-}$	calcd.	–14	92	–67	132	200	98		
	expt.	–9	87	–57	128	184	99[a]	93,94	
$[TcNF_4]^{-}$	calcd.	–47	–91	–25	–765	–1153	–571		
	expt.	–44	–107	–12	–734	–1129	–537	95	96
$[TcNCl_4]^{-}$	calcd.	2	17	–6	–610	–930	–450		
	expt.	0	6	–2	–561	–878	–402	97	98
$[TcNBr_4]^{-}$	calcd.	73	171	23	–548	–801	–421		
	expt.	69	145	32	–488	–743	–360	97	99
$[WOCl_4]^{-}$	calcd.	–209	–200	–213	–223	–347	–161		
	expt.	–229	–209	–239	-	-	-	100	
$[WOF_5]^{2-}$	calcd.	–391	–464	–354	–329	–473	–257		
	expt.	–368	–443	–330	–331	–469	–262	93,94	
$[WOBr_5]^{2-}$	calcd.	–201	–111	–246	–198	–313	–141		
	expt.	–172	–99[b]	–206[b]	-	-	–105	93,94	

$[ReNF_4]^-$	calcd.	–198	–351	–121	–2076	–3054	–1587		
	expt.	–206	–353	–132	–2117	–3079	–1637	101	
$[ReNCl_4]^-$	calcd.	–86	–99	–79	–1475	–2265	–1081		
	expt.	–78	–87	–73	–1544	–2263	–1184	102	103-105
$[ReNBr_4]^-$	calcd.	–3	82	–46	–1249	–1915	–917		
	expt.	3	67	–29	–1340	–1994	–1013	105	106
$[ReOBr_4]$	calcd.	–42	237	–182	–865	–1343	–626		
	expt.	–98	171	–232	-	-	-	107	
$[ReOF_5]^-$	calcd.	–350	–326	–362	–1809	–2682	–1372		
	expt.	–269	–282	–262	–1959	–2878	–1499	108	109
$[OsOF_5]$	calcd.	–299	–178	–360	–603	–911	–448		
	expt.	–324	–197	–387[c]	–627	–935[d]	–480	108	

[a] Expt. value for the perpendicular component obtained as $A_\perp = (3A_{iso} - A_{||})/2$. [b] Note that numerical data for $\Delta g_{||}$ and $\Delta g_\perp$ of $[WOBr_5]^{2-}$ had been exchanged in refs. 93, 94, as evident from the experimental g_{iso} value and also from our calculations. [c] Value averaged over two close g-tensor components. [d] Note that two digits in the $A_{||}$ value for $[OsOF_5]$ in ref. 108 had been exchanged (the -132.10^{-4} cm^{-1} should be -312.10^{-4} cm^{-1}).

However, let us first analyze the importance of scalar relativistic (SR) and spin-orbit (SO) effects on the computed EPR parameters of the smaller d^1 complexes. To this end we compare the 4c-mDKS data with a) those obtained by applying the corresponding Breit-Pauli operators to non-relativistic (NR) Kohn-Sham wavefunctions and with b) those calculated within the second-order perturbation 1c-DKH framework, using identical basis sets and exchange-correlation potentials. Figures 3 and 4 provide graphical comparisons for some selected systems (see also Tables S3, S4 in Supporting Information for detailed numerical data). Hence, it is obvious that scalar relativistic effects play a rather minor role for **g**-tensors of 4d complexes (SR effects are usually only a few ppt, up to ~14 ppt for $[TcNBr_4]^-$), while they

have a sizeable negative contribution to the **g**-shift components of 5d complexes, in particular for $\Delta g_{\parallel}$ (several tens of ppt up to −104 ppt in $[ReNBr_4]^-$, which corresponds to a decrease of the $\Delta g_{\parallel}$ value by ~50%; cf. Figure 3). Whereas the 1c-DKH $\Delta g_{\perp}$ values for the 4d complexes reproduce the experimental values very well, the computed "parallel" g-tensor component at this level is insufficiently negative (cf. Table S3 for PBE0-40HF/Dyall(TZ)/IGLO-III results). Here, a variational inclusion of SO coupling is necessary, as also demonstrated by our previous studies at the two-component DKH level.[40,48] Higher-order SO (HOSO) contributions to the **g**-tensor (beyond leading order in perturbation theory) become even more vital for the 5d complexes, where these effects are roughly an order of magnitude larger than for the 4d complexes and contribute to the $\Delta g_{\perp}$ component as well. For instance, HOSO contributions amount up to −180 ppt (-95 ppt) for $\Delta g_{\parallel}$ ($\Delta g_{\perp}$) in case of $[OsOF_5]$ (Figure 3).

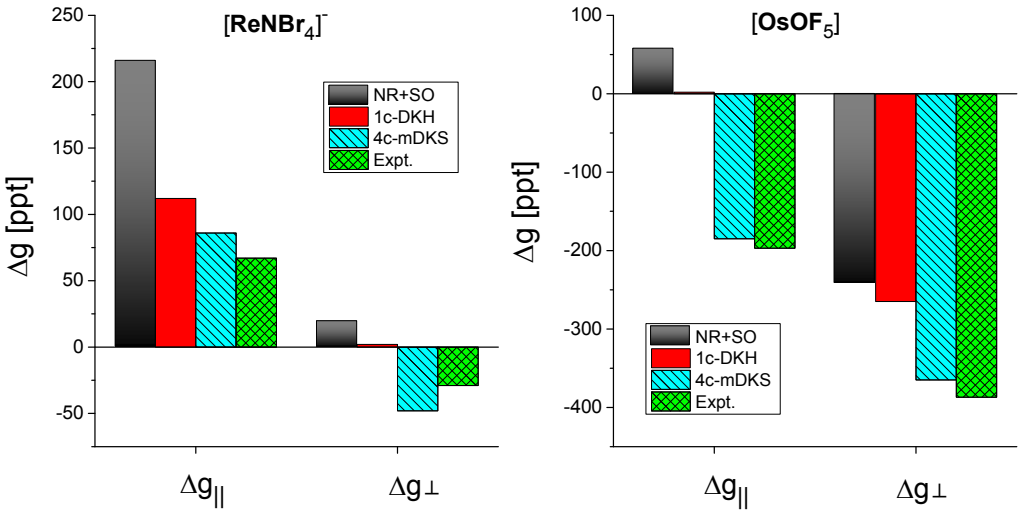

Figure 3. $\Delta g_{\parallel}$ and $\Delta g_{\perp}$ computed for $[ReNBr_4]^-$ and $[OsOF_5]$ within the one-component perturbation approach (1c-DKH) and at the four-component relativistic level (4c-mDKS) (cf. Computational Details) in comparison with experimental data (PBE0-40HF/Dyall(TZ)/IGLO-III results; cf. Table S3 in Supporting Information for numerical values). The results for non-relativistic wavefunctions and application of Breit-Pauli SO operators (denoted as "NR+SO") are given as well.

In contrast, metal hyperfine couplings are significantly affected by SR effects even for the 4d complexes, with enhancements of about 10–15% and 25–35% for $A_{\parallel}$ and $A_{\perp}$, respectively. As expected, this enhancement is even more pronounced for the 5d complexes (ca. 22–61% and 58–136% for $A_{\parallel}$ and $A_{\perp}$, respectively). Inclusion of leading-order SO corrections increases the absolute value of the HFCs further, more so for the 5d than for the 4d complexes. Interestingly, whereas the perturbational 1c-DKH+SO $A_{\parallel}$ values are already close to experiment, the corresponding $A_{\perp}$ data overshoot appreciably (Figure 4). Both **A**-tensor components are reproduced well at the 4c-mDKS level, indicating the importance of HOSO effects also for HFCs (more so for the 5d than for the 4d complexes).

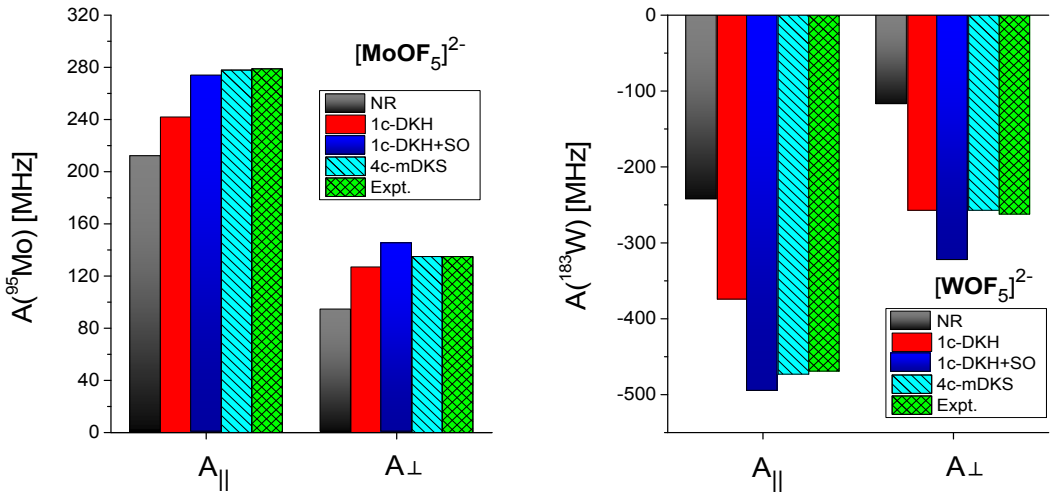

Figure 4. $A_{\parallel}$ and $A_{\perp}$ computed for $[MOF_5]^{2-}$ (M = Mo, W) at the one-component perturbational (1c-DKH) level, with and without inclusion of second-order SO corrections, and at the four-component relativistic level (4c-mDKS) (cf. Computational Details) in comparison with experimental data and non-relativistic results (PBE0-40HF/Dyall(TZ)/IGLO-III data; see also Table S4 in Supporting Information).

Further qualitative insight is obtained by scaling the speed of light, and thus also the SO integrals, in the 4c-mDKS calculations with different factors (see Computational Details). For the present 4d and 5d systems, the resulting curves are clearly nonlinear, which confirms the influence of *HOSO* effects.[48] As illustrative examples, Figure 5 shows the curves for both **Δg**

and **A**-tensor components for the two $5d^1$ complexes $[ReNBr_4]^-$ and $[OsOF_5]$. The nonlinear behavior is particularly obvious for the **g**-tensors, where the Re complex even exhibits a non-monotonous trend. We also see that the SO effects may go in either a positive or a negative direction, explaining the partly strange shapes of the curves. Somewhat smaller deviations from linearity are found for the HFCs, which indicates overall smaller HOSO effects, corroborating previous analyses at the two-component level by Verma and Autschbach.[54]

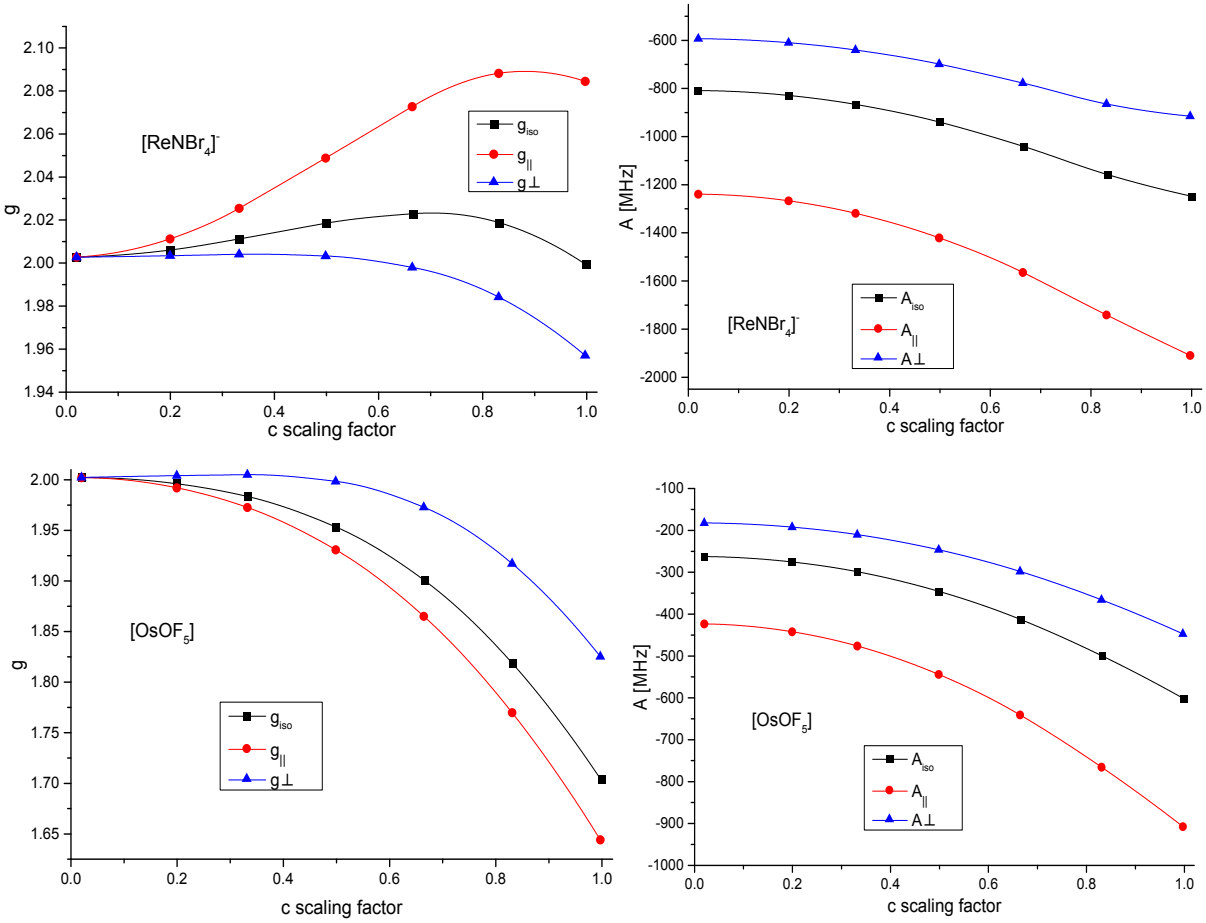

Figure 5. "Speed of light scaling" analyses (4c-mDKS level) for principal Δ**g**- and **A**-tensor components for $[ReNBr_4]^-$ and $[OsOF_5]$ (PBE0-40HF/Dyall(TZ)/IGLO-III results).

Larger iridium(II) and platinum(III) complexes

As an independent test and application of the selected PBE0-40HF/Dyall(TZ)/IGLO-III computational protocol, we have chosen a set of larger Ir(II) or Pt(III) complexes with $5d^7$ (S = ½) configuration, for which experimental EPR data are available, and which exhibit large **g**-

tensor anisotropies (see Figure 6 for the structures).[110-115] These larger complexes also demonstrate the efficiency of the 4c-mDKS approach, as they contain up to 133 atoms and 607 electrons in the case of $[PtI_2(IPr)_2]^+$. For this complex, we indeed reduced the computational effort by using the somewhat smaller Hirao/IGLO-II basis set combination (leading to 2960 Cartesian one-component GTOs). For comparative purposes, we have also computed a slightly truncated complex, where the isopropyl substituents of the "IPr" ligand (IPr = 1,3-bis(2,6-diisopropylphenyl)imidazole-2-ylidine) were replaced by methyl groups ($[PtI_2(IPr')_2]^+$, cf. Figure 6). In this case, we still compared with data for the larger Dyall(TZ)/IGLO-III combination and find only rather minor differences between the results obtained with these two basis sets (see Table 2). Truncation of $[PtI_2(IPr)_2]^+$ to $[PtI_2(IPr')_2]^+$ affects the results for both the **g**-shift and HFC **A**-tensor relatively little, consistent with the predominantly metal-centered spin density. In view of the good performance of the Hirao/IGLO-II basis sets for the smaller d^1 complexes (see above), we also included PBE0-40HF/Hirao/IGLO-II values for the other systems. They differ moderately from the Dyall(TZ)/IGLO-III data (Table 2).

As a further test of optimal EXX admixture, Table 2 compares principal components of the Δ**g**-shift and **A**-tensors for PBE, PBE0 and PBE0-40HF. Even for the very large **g**-tensor anisotropies of some of these systems, the dependence on the functional is not too pronounced (with the apparent exception of the Δg_{22} component in Pt(III) complexes; see Table 2). Hybrid functionals are better than PBE for the **g**-tensors, and the PBE0-40HF-based protocol appears to perform overall well (PBE0 appears to be in slightly better agreement only with the experimental Δg_{22} and Δg_{33} components for $[PtI_2(IPr)_2]^+$, but not for the isotropic g-shift values). Overall, the very large **g**-tensor anisotropies are reproduced well. Similarly, a surprisingly small dependence of the HFC components on EXX admixture is seen for these complexes, with even PBE reproducing the available tensor components reasonably well.

An interesting non-monotonic dependence of the **A**-tensor components on the EXX admixture is found for $[Pt(C_6Cl_5)_4]^-$ (Table 2), with PBE < PBE0 > PBE0-40HF. This trend is seen already at the DKH scalar relativistic level (Table S9 in Supporting Information). Whereas the overall metal spin density increases with larger EXX admixture (as expected), analyses of NPA atomic spin densities show that the hybridization between 6s and 5d AO contributions is more involved: the Pt 5d spin density increases monotonously, but the 6s spin density shows a small peak for PBE0 before decreasing for PBE0-40HF (see also Figure S1 for spin densities). Even very small changes in these 6s-type spin populations can affect the "direct" SOMO contributions to the metal HFC significantly, thus explaining the unexpected non-monotonous trend (which also extends to the Δg_{33} component; see Table 2).

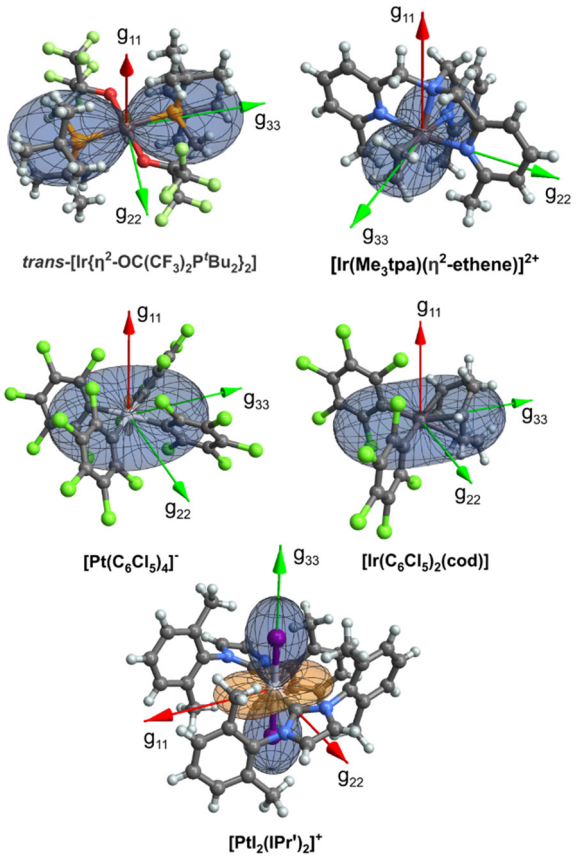

Figure 6. Visualization of the electronic Δ**g**-tensors (represented as polar plots of the $\Sigma_{i,j} r_i r_j \Delta g_{ij}$ function; blue isosurface = positive value, orange isosurface = negative value)[116] and their principal axes in selected Ir(II) and Pt(III) complexes. A green arrow indicates a positive *g*-shift component; a red one indicates a negative *g*-shift component.

Table 2. Experimental *vs.* calculated principal components of the Δ**g** (in ppt) and hyperfine **A**-tensors (in MHz) in larger Ir(II) and Pt(III) complexes. Calculations done at the 4c-mDKS level using different functionals and basis sets.

Complex	Method	Δg_{iso} [ppt]	Δg_{11} [ppt]	Δg_{22} [ppt]	Δg_{33} [ppt]	*M*	$A_{iso}(M)$ [MHz]	$A_{11}(M)$ [MHz]	$A_{22}(M)$ [MHz]	$A_{33}(M)$ [MHz]
trans-[Ir{η²-OC(CF_3)$_2$P^{t}Bu_2}$_2$]	PBE/Dyall(TZ)/IGLO-III	269	–140	206	741	^{193}Ir	5	–21	–9	47
	PBE0/Dyall(TZ)/IGLO-III	318	–184	211	927	^{193}Ir	–3	–49	–26	66
	PBE0-40HF/Dyall(TZ)/IGLO-III	336	–235	188	1055	^{193}Ir	–9	–67	–40	79
	PBE0-40HF/Hirao/IGLO-II	335	–246	168	1084	^{193}Ir	–12	–70	–44	79
	expt.[114]	358	–202	218	1058		-	-	-	-
[Ir(Me_3tpa)(η²-ethene)]$^{2+}$	PBE/Dyall(TZ)/IGLO-III	200	–46	190	457	^{193}Ir	136	90	147	171
	PBE0/Dyall(TZ)/IGLO-III	238	–41	223	530	^{193}Ir	131	86	144	163
	PBE0-40HF/Dyall(TZ)/IGLO-III	258	–38	240	573	^{193}Ir	127	82	140	159
	PBE0-40HF/Hirao/IGLO-II	261	–36	240	579	^{193}Ir	123	79	136	155
	expt.[113]	258	–27	263	538	^{193}Ir	-	-	-	138
[Ir(C_6Cl_5)$_2$(cod)]	PBE/Dyall(TZ)/IGLO-III	351	–147	488	713	^{193}Ir	463	438	470	481
	PBE0/Dyall(TZ)/IGLO-III	433	–143	639	802	^{193}Ir	447	409	460	470
	PBE0-40HF/Dyall(TZ)/IGLO-III	462	–128	664	850	^{193}Ir	424	384	437	451
	PBE0-40HF/Hirao/IGLO-II	454	–126	647	842	^{193}Ir	414	374	427	440
	expt.[110]	545	–149	788	998		-	-	-	-

Complex	Method	Δg_{iso} [ppt]	Δg_{11} [ppt]	Δg_{22} [ppt]	Δg_{33} [ppt]	*M*	$A_{iso}(M)$ [MHz]	$A_{11}(M)$ [MHz]	$A_{22}(M)$ [MHz]	$A_{33}(M)$ [MHz]
$[Pt(C_6Cl_5)_4]^-$	PBE/Dyall(TZ)/IGLO-III	206	–511	52	1078	^{195}Pt	7018	6315	6902	7838
	PBE0/Dyall(TZ)/IGLO-III	489	–344	826	986	^{195}Pt	7887	7029	8272	8360
	PBE0-40HF/Dyall(TZ)/IGLO-III	543	–330	927	1031	^{195}Pt	7507	6600	7940	7981
	PBE0-40HF/Hirao/IGLO-II	548	–323	931	1036	^{195}Pt	7345	6445	7773	7816
	expt.[112]	594	–400	1005	1177	^{195}Pt	7322	6375	7735	7855
$[PtI_2(IPr')_2]^+$	PBE/Dyall(TZ)/IGLO-III	–220	–1244	–1020	1604	^{195}Pt	431	182	585	524
						^{127}I[a]	250	18	–53	786
	PBE0/Dyall(TZ)/IGLO-III	–85	–1064	–767	1575	^{195}Pt	472	173	713	531
						^{127}I[a]	252	57	–49	748
	PBE0-40HF/Dyall(TZ)/IGLO-III	7	–940	–533	1493	^{195}Pt	520	152	872	536
						^{127}I[a]	244	91	–42	685
	PBE0-40HF/Hirao/IGLO-II	–1	–960	–553	1511	^{195}Pt	476	131	805	491
						^{127}I[b]	256	92	–40	718
	expt.[111,c]	–15	–933	–722	1610	^{195}Pt	-	-	-	500
						^{127}I	-	-	-	802

Complex	Method	Δg_{iso} [ppt]	Δg_{11} [ppt]	Δg_{22} [ppt]	Δg_{33} [ppt]	*M*	$A_{iso}(M)$ [MHz]	$A_{11}(M)$ [MHz]	$A_{22}(M)$ [MHz]	$A_{33}(M)$ [MHz]
$[PtI_2(IPr)_2]^+$	PBE0-40HF/Hirao/IGLO-II	19	–932	–508	1497	^{195}Pt	494	136	840	507
						^{127}I[b]	252	99	–41	697
	expt.[111]	–15	–933	–722	1610	^{195}Pt	-	-	-	500
						^{127}I	-	-	-	802

[a] Dyall(TZ) basis set used on iodine. [b] Hirao basis set used on iodine. [c] Expt. values for $[PtI_2(IPr)_2]^+$.

Table 3. Comparison of Δ**g**-shift components (in ppt) computed at the 1c-DKH and 4c-mDKS relativistic level, respectively.[a] Higher-order spin-orbit (*HOSO*) effects estimated from the difference between 4c-mDKS and 1c-DKH data.

		Δg_{iso} [ppt]	Δg_{11} [ppt]	Δg_{22} [ppt]	Δg_{33} [ppt]
trans-[Ir{η²-OC(CF$_3$)$_2$P^{t}Bu$_2$}$_2$]	1c-DKH	744	343	410	1477
	4c-mDKS	335	–246	168	1084
	expt.[114]	358	–202	218	1058
	HOSO	*–409*	*–589*	*–242*	*–393*
[Ir(Me$_3$tpa)(η²-ethene)]$^{2+}$	1c-DKH	377	47	450	634
	4c-mDKS	261	–36	240	579
	expt.[113]	258	–27	263	538
	HOSO	*–116*	*–83*	*–210*	*–55*
[Ir(C$_6$Cl$_5$)$_2$(cod)]	1c-DKH	705	23	976	1116
	4c-mDKS	454	–126	647	842
	expt.[110]	545	–149	788	998
	HOSO	*–251*	*–149*	*–329*	*–274*
[Pt(C$_6$Cl$_5$)$_4$]$^-$	1c-DKH	1427	13	2051	2217
	4c-mDKS	548	–323	931	1036
	expt.[112]	594	–400	1005	1177
	HOSO	*–879*	*–336*	*–1120*	*–1181*
[PtI$_2$(IPr')$_2$]$^+$	1c-DKH	1708	219	1170	3736
	4c-mDKS	–1	–960	–553	1511
	expt.[111,b]	–15	–933	–722	1610
	HOSO	*–1709*	*–1179*	*–1723*	*–2225*

[a] Results obtained at the PBE0-40HF/Hirao/IGLO-II level (cf. Computational details). [b] Expt. values for [PtI$_2$(IPr)$_2$]$^+$.

In view of the extremely large **g**-tensor anisotropies for several of the complexes in Table 2, assessment of the importance of *HOSO* effects for these tensors is of particular interest. Table 3 compares 4c-mDKS and 1c-DKH results (using identical functionals and basis sets) and

estimates the *HOSO* contributions from the difference. We first of all note, that the *HOSO* contributions amount to several hundreds of ppt for the three Ir complexes and to thousands of ppt for the two Pt complexes, and they thus exceed by far the dependence on the functional (cf. Table 2). We even see changes of sign for some tensor components (for instance, the Δg_{11} component is systematically overestimated at the 1c-DKH level) and overall fundamental modifications of the entire tensor (as indicated by the percentage contributions in Table 3). In all five test cases, the 4c-mDKS results exhibit significantly better agreement with experiment than the 1c-DKH data.

Further insight into the *HOSO* effects may again be obtained from a "*c* scaling" analysis (Figure 7, one Ir and one Pt complex shown, additional plots are in Figure S2 in Supporting Information), for both Δ**g**-shift and HFC **A**-tensor components. All plots are clearly nonlinear and confirm the need to include relativistic effects variationally to reproduce the correct sign and magnitude of EPR parameters in these complexes. We also note that SO effects may change the sign for a given HFC tensor component, as seen for A_{33} of *trans*-[Ir{η^2-$OC(CF_3)_2P^tBu_2$}$_2$] (cf. Figure 7). Similarly, scalar relativistic 1c-DKH calculations are not able to reproduce the positive sign for all $\mathbf{A}(^{195}Pt)$-tensor components of $[PtI_2(IPr)_2]^+$ (cf. Table 2 and Table S9), and inclusion of only leading-order SO corrections overshoots the A_{33} value by more than 100% (cf. Table S11 in Supporting Information).

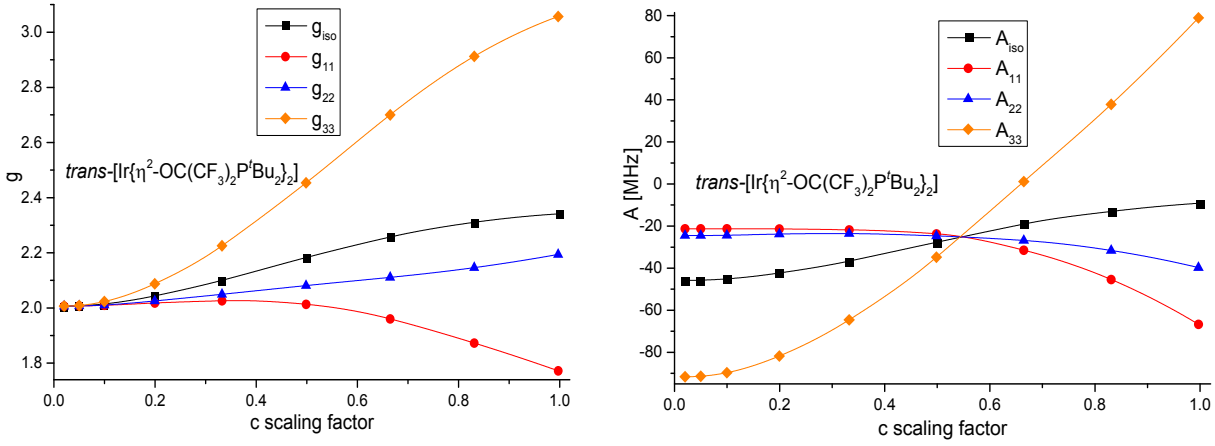

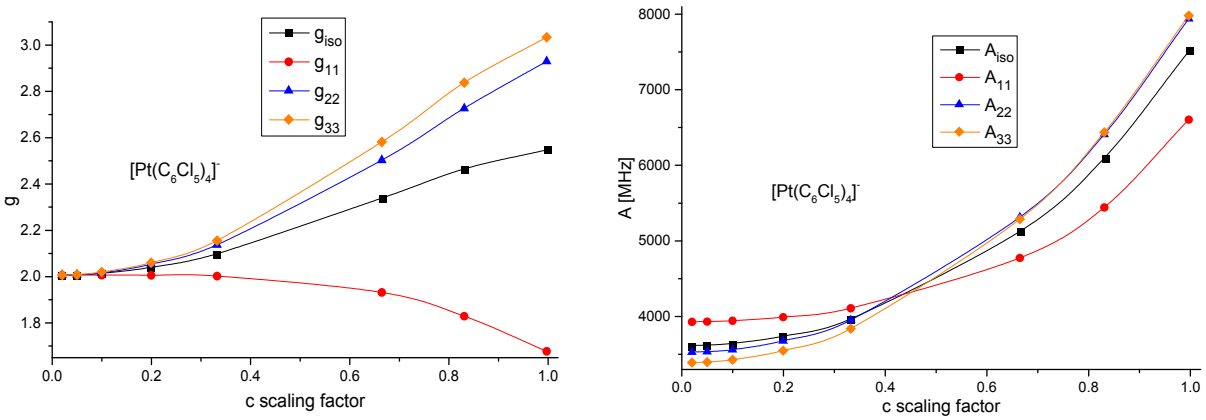

Figure 7. "Speed of light scaling" analyses of principal **g**- and **A**-tensor components at 4c-mDKS level for *trans*-[Ir{η²-OC(CF$_3$)$_2$P^{t}Bu$_2$}$_2$] and [Pt(C$_6$Cl$_5$)$_4$]$^-$ (PBE0-40HF/Dyall(TZ)/IGLO-III results).

We finally note that the present implementation is able to handle heavy-metal complexes with more than 100 atoms and 2000 (scalar one-component) basis functions in affordable time. For instance, the 4c-mDKS calculations for the largest complex [PtI$_2$(IPr)$_2$]$^+$ with 133 atoms and 2960 basis functions required ~14 days on 24 CPUs, Intel Xeon 2.67GHz, with the three spin-unrestricted SCF calculations done in parallel (each SCF running on 8 CPUs).

Conclusions

This work reports the implementation, and first applications of global hybrid functionals in four-component relativistic calculations of electronic **g**- and hyperfine-coupling **A**-tensors. The efficiency of the implementation in the ReSpect program allows computations for rather large complexes and thus makes the method available for interesting applications in a wide range of fields.

Systematic benchmarking of hybrid functionals and basis sets on a series of 17 small 4d^1 and 5d^1 complexes suggested a computational protocol (mDKS/PBE0-40HF/Dyall(TZ)/IGLO-III) that performed well for both **g**- and HFC **A**-tensors. In general, the need for appreciable exact-exchange admixture in hybrid functionals was apparent, in particular for the HFCs.

Application of this protocol to larger Ir(II) and Pt(III) complexes with very large **g**-tensor anisotropies confirmed its applicability and demonstrated the importance of spin-orbit effects beyond leading order in perturbation theory. This holds particularly true for the extreme **g**-shift anisotropies, where the higher-order SO effects can easily amount to several hundreds or even thousands of ppt and change the appearance of the tensor fundamentally.

ASSOCIATED CONTENT

Supporting Information. Tables with numerical results for **g**-tensors and hyperfine **A**-tensors at various computational levels, statistical data evaluations, spin-density plots and atomic spin-density analyses, "c-scaling" analyses, visualization of **g**-tensors and their principal axes at different relativistic levels and Cartesian coordinates of all investigated complexes. This material is available free of charge via the Internet at http://pubs.acs.org.

AUTHOR INFORMATION

Corresponding Authors

*E-mail: peter.hrobarik@tu-berlin.de; martin.kaupp@tu-berlin.de

Telephone: +49 30 314 79682

ACKNOWLEDGMENTS

The authors acknowledge support from the Berlin DFG excellence cluster on Unifying Concepts in Catalysis (UniCat). S. G. is also indebted to the German National Academic Foundation (Studienstiftung des deutschen Volkes) for financial support. The work in Tromsø was supported from the Research Council of Norway through a Centre of Excellence Grant and project grants (Grant No. 179568, 214095, 177558, and 191251) and the European Research Council starting grant (Grant No. 279619).

References

(1) Abragam, A.; Bleaney, B., *Electron Paramagnetic Resonance of Transition Ions*; Clarendon Press: Oxford, U.K., 1970.

(2) Atherton, N. M., *Electron Spin Resonance: Theory and Applications*; Ellis Horwood Ltd.: Chichester, 1973.

(3) Harriman, J. E., *Theoretical Foundations of Electron Spin Resonance*; Academic press: New York, 1978.

(4) Kaupp, M.; Bühl, M.; Malkin, V. G., *Calculation of NMR and EPR Parameters: Theory and Applications*. Wiley-VCH: Weinheim, 2004.

(5) Lund, A.; Shiotani, M., *EPR Spectroscopy of Free Radicals in Solids. Trends in Methods and Applications*. Kluwer: Dordrecht, 2003.

(6) Chiesa, M.; Giamello, E.; Che, M. EPR Characterization and Reactivity of Surface-Localized Inorganic Radicals and Radical Ions. *Chem. Rev.* **2010**, *110*, 1320-1347.

(7) Kahn, O., *Molecular Magnetism*; Wiley-VCH: New York, 1993.

(8) Miller, J. S.; Drillon, M., *Magnetism: Molecules to Materials*; Wiley-VCH: New York, 2001.

(9) Gatteschi, D. Molecular Magnetism - a Basis for New Materials. *Adv. Mater.* **1994**, *6*, 635-645.

(10) Miller, J. S.; Epstein, A. J. Organic and Organometallic Molecular Magnetic Materials - Designer Magnets. *Angew. Chem. Int. Ed.* **1994**, *33*, 385-415.

(11) Hanson, G.; Berliner, L., *Metals in Biology: Applications of High-Resolution EPR to Metalloenzymes*. Springer-Verlag: New York, 2010.

(12) Solomon, E. I.; Lever, A. B., *Inorganic Electronic Structure and Spectroscopy, Volume I: Methodology*. John Wiley and Sons, Inc.: New York, 1999.

(13) Neese, F. Quantum Chemical Calculations of Spectroscopic Properties of Metalloproteins and Model Compounds: EPR and Mössbauer Properties. *Current Opinion in Chemical Biology* **2003**, *7*, 125–135.

(14) Hrobárik, P.; Kaupp, M.; Riedel, S. Is Allred's $[Hg(cyclam)]^{3+}$ a True Mercury(III) Complex? *Angew. Chem. Int. Ed.* **2008**, *47*, 8631-8633.

(15) Scheibel, M. G.; Askevold, B.; Heinemann, F. W.; Reijerse, E. J.; de Bruin, B.; Schneider, S. Closed-Shell and Open-Shell Square-Planar Iridium Nitrido Complexes. *Nat. Chem.* **2012**, *4*, 552-558.

(16) van der Eide, E. F.; Yang, P.; Walter, E. D.; Liu, T. B.; Bullock, R. M. Dinuclear Metalloradicals Featuring Unsupported Metal-Metal Bonds. *Angew. Chem. Int. Ed.* **2012**, *51*, 8361-8364.

(17) Schwamm, R. J.; Harmer, J. R.; Lein, M.; Fitchett, C. M.; Granville, S.; Coles, M. P. Isolation and Characterization of a Bismuth(II) Radical. *Angew. Chem. Int. Ed.* **2015**, *54*, 10630-10633.

(18) Chibotaru, L. F.; Ungur, L. Ab Initio Calculation of Anisotropic Magnetic Properties of Complexes. I. Unique Definition of Pseudospin Hamiltonians and Their Derivation. *J. Chem. Phys.* **2012**, *137*, 64112.

(19) Bolvin, H. An Alternative Approach to the g-Matrix: Theory and Applications. *ChemPhysChem* **2006**, *7*, 1575–1589.

(20) Vancoillie, S.; Malmqvist, P.-A.; Pierloot, K. Calculation of EPR g-Tensors for Transition-Metal Complexes Based on Multiconfigurational Perturbation Theory (CASPT2). *ChemPhysChem* **2007**, *8*, 1803–1815.

(21) Gendron, F.; Pritchard, B.; Bolvin, H.; Autschbach, J. Magnetic Resonance Properties of Actinyl Carbonate Complexes and Plutonyl(VI)-tris-Nitrate. *Inorg. Chem.* **2014**, *53*, 8577-8592.

(22) Sharkas, K.; Pritchard, B.; Autschbach, J. Effects from Spin–Orbit Coupling on Electron–Nucleus Hyperfine Coupling Calculated at the Restricted Active Space Level for Kramers Doublets. *J. Chem. Theory Comput.* **2015**, *11*, 538–549.

(23) Yanai, T.; Kurashige, Y.; Mizukami, W.; Chalupsky, J.; Lan, T. N.; Saitow, M. Density Matrix Renormalization Group for ab initio Calculations and Associated Dynamic Correlation Methods: A Review of Theory and Applications. *Int. J. Quantum Chem.* **2015**, *115*, 283-299.

(24) Lan, T. N.; Kurashige, Y.; Yanai, T. Toward Reliable Prediction of Hyperfine Coupling Constants Using Ab Initio Density Matrix Renormalization Group Method: Diatomic ^{2}S and Vinyl Radicals as Test Cases. *J. Chem. Theory Comput.* **2014**, *10*, 1953-1967.

(25) Gauss, J.; Kallay, M.; Neese, F. Calculation of Electronic g-Tensors using Coupled Cluster Theory. *J. Phys. Chem. A* **2009**, *113*, 11541-11549.

(26) Vad, M. S.; Pedersen, M. N.; Norager, A.; Jensen, H. J. A. Correlated Four-Component EPR g-Tensors for Doublet Molecules. *J. Chem. Phys.* **2013**, *138,* 214106.

(27) Sasmal, S.; Pathak, H.; Nayak, M. K.; Vaval, N.; Pal, S. Relativistic Extended-Coupled-Cluster Method for the Magnetic Hyperfine Structure Constant. *Phys. Rev. A* **2015**, *91,* 022512.

(28) Malkina, O. L.; Vaara, J.; Schimmelpfennig, B.; Munzarová, M.; Malkin, V. G.; Kaupp, M. Density Functional Calculations of Electronic g -Tensors Using Spin−Orbit Pseudopotentials and Mean-Field All-Electron Spin−Orbit Operators. *J. Am. Chem. Soc.* **2000**, *122*, 9206–9218.

(29) Neese, F. Prediction of Electron Paramagnetic Resonance g-Values using Coupled Perturbed Hartree-Fock and Kohn-Sham Theory. *J. Chem. Phys.* **2001**, *115*, 11080-11096.

(30) Kaupp, M.; Reviakine, R.; Malkina, O. L.; Arbuznikov, A.; Schimmelpfennig, B.; Malkin, V. G. Calculation of Electronic g-Tensors for Transition Metal Complexes Using Hybrid Density Functionals and Atomic Meanfield Spin-Orbit Operators. *J. Comput. Chem.* **2002**, *23*, 794–803.

(31) Neese, F. Metal and Ligand Hyperfine Couplings in Transition Metal Complexes: The Effect of Spin-Orbit Coupling as Studied by Coupled Perturbed Kohn-Sham Theory. *J. Chem. Phys.* **2003**, *118*, 3939-3948.

(32) Arbuznikov, A. V.; Vaara, J.; Kaupp, M. Relativistic Spin-Orbit Effects on Hyperfine Coupling Tensors by Density-Functional Theory. *J. Chem. Phys.* **2004**, *120*, 2127-2139.

(33) Manninen, P.; Vaara, J.; Ruud, K. Perturbational Relativistic Theory of Electron Spin Resonance g-Tensor. *J. Chem. Phys.* **2004**, *121*, 1258–1265.

(34) Rinkevicius, Z.; de Almeida, K. J.; Oprea, C. I.; Vahtras, O.; Agren, H.; Ruud, K. Degenerate Perturbation Theory for Electronic g Tensors: Leading-Order Relativistic Effects. *J. Chem. Theory Comput.* **2008**, *4*, 1810-1828.

(35) van Lenthe, E.; Wormer, P. E. S.; van der Avoird, A. Density Functional Calculations of Molecular g-Tensors in the Zero-Order Regular Approximation for Relativistic Effects. *J. Chem. Phys.* **1997**, *107*, 2488–2498.

(36) van Lenthe, E.; van der Avoird, A.; Wormer, P. E. S. Density Functional Calculations of Molecular Hyperfine Interactions in the Zero Order Regular Approximation for Relativistic Effects. *J. Chem. Phys.* **1998**, *108*, 4783–4796.

(37) Schreckenbach, G.; Ziegler, T. Density Functional Calculations of NMR Chemical Shifts and ESR g-Tensors. *Theor. Chem. Acc.* **1998**, *99*, 71–82.

(38) Neyman, K. M.; Ganyushin, D. I.; Matveev, A. V.; Nasluzov, V. A. Calculation of Electronic g -Tensors Using a Relativistic Density Functional Douglas−Kroll Method. *J. Phys. Chem. A* **2002**, *106*, 5022–5030.

(39) Malkin, I.; Malkina, O. L.; Malkin, V. G.; Kaupp, M. Relativistic Two-Component Calculations of Electronic g-Tensors that Include Spin Polarization. *J. Chem. Phys.* **2005**, *123*, 244103.

(40) Hrobárik, P.; Malkina, O. L.; Malkin, V. G.; Kaupp, M. Relativistic Two-Component Calculations of Electronic g-tensor for Oxo-Molybdenum(V) and Oxo-Tungsten(V) Complexes: The Important Role of Higher-Order Spin-Orbit Contributions. *Chem. Phys.* **2009**, *356*, 229–235.

(41) Komorovský, S.; Repiský, M.; Malkina, O. L.; Malkin, V. G.; Malkin, I.; Kaupp, M. Resolution of Identity Dirac-Kohn-Sham Method using the Large Component Only: Calculations of g-Tensor and Hyperfine Tensor. *J. Chem. Phys.* **2006**, *124,* 084108.

(42) Repiský, M.; Komorovský, S.; Malkin, E.; Malkina, O. L.; Malkin, V. G. Relativistic Four-Component Calculations of Electronic g-Tensors in the Matrix Dirac-Kohn-Sham Framework. *Chem. Phys. Lett.* **2010**, *488*, 94-97.

(43) Malkin, E.; Repiský, M.; Komorovský, S.; Mach, P.; Malkina, O. L.; Malkin, V. G. Effects of Finite-Size Nuclei in Relativistic Four-Component Calculations of Hyperfine Structure. *J. Chem. Phys.* **2011**, *134*, 044111.

(44) Malkin, I.; Malkina, O. L.; Malkin, V. G.; Kaupp, M. Scalar Relativistic Calculations of Hyperfine Coupling Tensors using the Douglas–Kroll–Hess Method. *Chem. Phys. Lett.* **2004**, *396*, 268–276.

(45) Wolf, A.; Reiher, M. Exact Decoupling of the Dirac Hamiltonian. III. Molecular Properties. *J. Chem. Phys.* **2006**, *124*, 64102.

(46) Reiher, M. Douglas-Kroll-Hess Theory: a Relativistic Electrons-Only Theory for Chemistry. *Theor. Chem. Acc.* **2006**, *116*, 241-252.

(47) Sandhoefer, B.; Neese, F. One-Electron Contributions to the g-Tensor for Second-Order Douglas–Kroll–Hess Theory. *J. Chem. Phys.* **2012**, *137*, 94102.

(48) Hrobárik, P.; Repiský, M.; Komorovský, S.; Hrobáriková, V.; Kaupp, M. Assessment of Higher-Order Spin–Orbit Effects on Electronic g-tensors of d^1 Transition-Metal Complexes by Relativistic Two- and Four-Component Methods. *Theor. Chem. Acc.* **2011**, *129*, 715–725.

(49) Fritscher, J.; Hrobárik, P.; Kaupp, M. Computational Studies of EPR Parameters for Paramagnetic Molybdenum Complexes. I. Method Validation on Small and Medium-Sized Systems. *J. Phys. Chem. B* **2007**, *111*, 4616–4629.

(50) Fritscher, J.; Hrobárik, P.; Kaupp, M. Computational Studies of EPR Parameters for Paramagnetic Molybdenum Complexes. II. Larger Mo^V Systems Relevant to Molybdenum Enzymes. *Inorg. Chem.* **2007**, *46*, 8146–8161.

(51) Munzarová, M. L.; Kubáček, P.; Kaupp, M. Mechanisms of EPR Hyperfine Coupling in Transition Metal Complexes. *J. Am. Chem. Soc.* **2000**, *122*, 11900-11913.

(52) Munzarová, M.; Kaupp, M. A Critical Validation of Density Functional and Coupled-Cluster Approaches for the Calculation of EPR Hyperfine Coupling Constants in Transition Metal Complexes. *J. Phys. Chem. A* **1999**, *103*, 9966-9983.

(53) Hrobárik, P.; Reviakine, R.; Arbuznikov, A. V.; Malkina, O. L.; Malkin, V. G.; Kôhler, F. H.; Kaupp, M. Density Functional Calculations of NMR Shielding Tensors for Paramagnetic Systems with Arbitrary Spin Multiplicity: Validation on 3d Metallocenes. *J. Chem. Phys.* **2007**, *126,* 024107.

(54) Verma, P.; Autschbach, J. Relativistic Density Functional Calculations of Hyperfine Coupling with Variational versus Perturbational Treatment of Spin–Orbit Coupling. *J. Chem. Theory Comput.* **2013**, *9*, 1932–1948.

(55) Verma, P.; Autschbach, J. Variational versus Perturbational Treatment of Spin–Orbit Coupling in Relativistic Density Functional Calculations of Electronic g Factors: Effects from Spin-Polarization and Exact Exchange. *J. Chem. Theory Comput.* **2013**, *9*, 1052–1067.

(56) Autschbach, J. Relativistic Calculations of Magnetic Resonance Parameters: Background and Some Recent Developments. *Philos. Trans. R. Soc., A* **2014**, *372*, 20120489.

(57) ReSpect, Relativistic Spectroscopy DFT program of authors: Repiský, M.; Komorovský, S.; Malkin, V. G.; Malkina, O. L.; Kaupp, M.; Ruud, K. with contributions from Bast, R.; Ekstrom, U.; Kadek, M.; Knecht, S.; Konečný, L.; Malkin, E.; Malkin-Ondík, I.; version 3.4.2, 2015; available from http://www.respectprogram.org (accessed on April 12, 2015).

(58) Kutzelnigg, W. Basis Set Expansion of the Dirac Operator without Variational Collapse. *Int. J. Quantum Chem.* **1984**, *25*, 107–129.

(59) Stanton, R. E.; Havriliak, S. Kinetic Balance: A Partial Solution to the Problem of Variational Safety in Dirac Calculations. *J. Chem. Phys.* **1984**, *81*, 1910–1918.

(60) van Wüllen, C. Spin Densities in Two-Component Relativistic Density Functional Calculations: Noncollinear vs. Collinear Approach. *J. Comput. Chem.* **2002**, *23*, 779–785.

(61) Jayatilaka, D. Electron Spin Resonance g-Tensors from General Hartree–Fock Calculations. *J. Chem. Phys.* **1998**, *108*, 7587–7594.

(62) Neese, F. Efficient and Accurate Approximations to the Molecular Spin-Orbit Coupling Operator and Their Use in Molecular g-Tensor Calculations. *J. Chem. Phys.* **2005**, *122*, 034107.

(63) Frisch, M. J.; Trucks, G. W.; Schlegel, H. B.; Scuseria, G. E.; Robb, M. A.; Cheeseman, J. R.; Scalmani, G.; Barone, V.; Mennucci, B.; Petersson, G. A.; *et al.* Gaussian 09, revision D.01; Gaussian Inc.: Wallingford, CT, 2009.

(64) Perdew, J. P.; Burke, K.; Ernzerhof, M. Generalized Gradient Approximation Made Simple. *Phys. Rev. Lett.* **1996**, *77*, 3865–3868.

(65) Adamo, C.; Barone, V. Toward Chemical Accuracy in the Computation of NMR Shieldings: the PBE0 Model. *Chem. Phys. Lett.* **1998**, *298*, 113-119.

(66) Andrae, D.; Haussermann, U.; Dolg, M.; Stoll, H.; Preuss, H. Energy-Adjusted Ab-Initio Pseudopotentials for the 2nd and 3rd Row Transition-Elements. *Theor. Chim. Acta.* **1990**, *77*, 123-141.

(67) Weigend, F.; Ahlrichs, R. Balanced Basis Sets of Split Valence, Triple Zeta Valence and Quadruple Zeta Valence Quality for H to Rn: Design and Assessment of Accuracy. *Phys. Chem. Chem. Phys.* **2005**, *7*, 3297–3305.

(68) Grimme, S.; Antony, J.; Ehrlich, S.; Krieg, H. A Consistent and Accurate Ab Initio Parametrization of Density Functional Dispersion Correction (DFT-D) for the 94 Elements H-Pu. *J. Chem. Phys.* **2010**, *132*, 154104.

(69) Grimme, S.; Ehrlich, S.; Goerigk, L. Effect of the Damping Function in Dispersion Corrected Density Functional Theory. *J. Comput. Chem.* **2011**, *32*, 1456-1465.

(70) Malkin, V. G.; Malkina, O. L.; Reviakine, R.; Arbuznikov, A. V.; Kaupp, M.; Schimmelpfennig, B.; Malkin, I.; Repiský, M.; Komorovský, S.; Hrobárik, P.; Malkin, E.; Helgaker, T.; Ruud, K. *MAG-ReSpect*, version 2.3; 2010.

(71) Schimmelpfennig, B. *AMFI, an Atomic Mean-Field Integral Program*, Stockholm University: Stockholm, Sweden, 1996.

(72) Malkin, E.; Malkin, I.; Malkina, O. L.; Malkin, V. G.; Kaupp, M. Scalar Relativistic Calculations of Hyperfine Coupling Tensors using the Douglas-Kroll-Hess Method with a Finite-Size Nucleus Model. *Phys. Chem. Chem. Phys.* **2006**, *8*, 4079-4085.

(73) Dyall, K. G. Relativistic Double-Zeta, Triple-Zeta, and Quadruple-Zeta Basis Sets for the 5d Elements Hf-Hg. *Theor. Chem. Acc.* **2004**, *112*, 403–409.

(74) Dyall, K. G. Relativistic Double-Zeta, Triple-Zeta, and Quadruple-Zeta Basis Sets for the 4d Elements Y-Cd. *Theor. Chem. Acc.* **2007**, *117*, 483-489.

(75) Dyall, K. G. Relativistic Double-Zeta, Triple-Zeta, and Quadruple-Zeta Basis Sets for the Actinides Ac-Lr. *Theor. Chem. Acc.* **2007**, *117*, 491-500.

(76) Dyall, K. G.; Gomes, A. S. P. Revised Relativistic Basis Sets for the 5d Elements Hf-Hg. *Theor. Chem. Acc.* **2010**, *125*, 97-100.

(77) Nakajima, T.; Hirao, K. Accurate Relativistic Gaussian Basis Sets Determined by the Third-Order Douglas–Kroll Approximation with a Finite-Nucleus Model. *J. Chem. Phys.* **2002**, *116*, 8270–8275.

(78) Kutzelnigg, W.; Fleischer, U.; Schindler, M. The IGLO-Method: Ab-initio Calculation and Interpretation of NMR Chemical Shifts and Magnetic Susceptibilities. In *NMR Basic Principles and Progress*, Diehl, P.; Fluck, E.; Günther, H.; Kosfeld, R.; Seelig, J., Eds. Springer-Verlag: Berlin, 1991; Vol. 213, pp 165–262.

(79) Becke, A. D. Density-Functional Exchange-Energy Approximation with Correct Asymptotic Behavior. *Phys. Rev. A* **1988**, *38*, 3098–3100.

(80) Perdew, J. P.; Wang, Y. Accurate and Simple Density Functional for the Electronic Exchange Energy: Generalized Gradient Approximation. *Phys. Rev. B* **1986**, *33*, 8800–8802.

(81) Becke, A. D. Density-Functional Thermochemistry. III. The Role of Exact Exchange. *J. Chem. Phys.* **1993**, *98*, 5648–5652.

(82) Stephens, P. J.; Devlin, F. J.; Chabalowski, C. F.; Frisch, M. J. Ab-Initio Calculation of Vibrational Absorption and Circular-Dichroism Spectra Using Density-Functional Force-Fields. *J. Phys. Chem.* **1994**, *98*, 11623-11627.

(83) Lebedev, V. I. One Type of Quadrature Formulas of Algebraic Multiple Precision for Sphere. *Dokl. Akad. Nauk. SSSR* **1976**, *231*, 32-34.

(84) Neese, F. The ORCA Program System. *Wires. Comput. Mol. Sci.* **2012**, *2*, 73-78.

(85) Remenyi, C.; Kaupp, M. Where Is the Spin? Understanding Electronic Structure and g-Tensors for Ruthenium Complexes with Redox-Active Quinonoid Ligands. *J. Am. Chem. Soc.* **2005**, *127*, 11399-11413.

(86) Remenyi, C.; Reviakine, R.; Kaupp, M. Density Functional Study of EPR Parameters and Spin-Density Distribution of Azurin and Other Blue Copper Proteins. *J. Phys. Chem. B* **2007**, *111*, 8290-8304.

(87) Patchkovskii, S.; Ziegler, T. Prediction of EPR g-Tensors of Transition Metal Complexes using Density Functional Theory: First Applications to Some Axial d^1 MEX_4 Systems. *J. Chem. Phys.* **1999**, *111*, 5730–5740.

(88) Schmitte, J.; Friebel, C.; Weller, F.; Dehnicke, K. Synthese, IR- und EPR-Spektren sowie die Kristallstruktur von $(PPh_3Me)_2[MoNCl_4]$. *Z. Anorg. Allg. Chem.* **1982**, *495*, 148–156.

(89) Sunil, K. K.; Rogers, M. T. ESR studies of Some Oxotetrahalo Complexes of Vanadium(IV) and Molybdenum(V). *Inorg. Chem.* **1981**, *20*, 3283–3287.

(90) Garner, C. D.; Hill, L. H.; Mabbs, F. E.; McFadden, D. L.; McPhail, A. T. Crystal and Molecular Structure, Electron Spin Resonance, and Electronic Spectrum of Tetraphenylarsonium Tetrachloro-Oxomolybdenum(V). *J. Chem. Soc., Dalton Trans.* **1977**, 853–858.

(91) Boorman, P. M.; Garner, C. D.; Mabbs, F. E. Formation of and Equilibria between Some 5-Coordinate and 6-Coordinate Chloro-Oxomolybdenum(V) Complexes in Dichloromethane. *J. Chem. Soc., Dalton Trans.* **1975**, 1299-1306.

(92) Manoharan, P. T. Ligand Hyperfine Interactions in Molybdenyl and Chromyl Halide Complexes. *J. Chem. Phys.* **1968**, *49*, 5510–5519.

(93) van Kemenade, J. T. C., *Ligand Hyperfine Interactions in Oxyhalides of Pentavalent Chromium, Molybdenum and Tungsten*; Dissertation, Technical University Delft: Delft, Netherland, 1970.

(94) van Kemenade, J. T. C. Ligand Hyperfine Interactions in Oxyhalides of Pentavalent Chromium, Molybdenum and Tungsten. *Recl. Trav. Chim. Pays-Bas* **1973**, *92*, 1102-1120.

(95) Baldas, J.; Boas, J. F.; Bonnyman, J. Preparation and Properties of Nitridotechnetic(VI) Acid. I. Observation of the ESR Spectrum of the $[TcNF_4]^-$ Anion in Hydrofluoric Acid Solution. *Aust. J. Chem.* **1989**, *42*, 639–648.

(96) Baldas, J.; Boas, J. F.; Ivanov, Z.; James, B. D. EPR Evidence for the Formation of the Six-Coordinate Pentafluoronitridotechnetate(VI) Anion in Solution. *Transition Met. Chem.* **1997**, *22*, 74-78.

(97) Baldas, J.; Boas, J. F.; Bonnyman, J.; Williams, G. A. Studies of Technetium Complexes. The Preparation, Characterisation, and ESR Spectra of Salts of Tetrachloro- and Tetrabromo-Nitridotechnetate(VI): Crystal Structure of Tetraphenylarsonium Tetrachloronitridotechnetate(VI). *J. Chem. Soc., Dalton Trans.* **1984**, 2395–2400.

(98) Kirmse, R.; Köhler, K.; Abram, U.; Böttcher, R.; Golič, L.; de Boer, E. Single-crystal EPR on $(Ph_4As)[TcNCl_4/TcOCl_4]$ and Crystal Structure of $(Ph_4As)[TcOCl_4]$. *Chem. Phys.* **1990**, *143*, 75–82.

(99) Kirmse, R.; Stach, J.; Abram, U. $[TcNBr_{4-p}Cl_p]^-$ (p = 1–3) Nitridotechnetate(VI) Mixed-Ligand Complexes. An EPR study. *Inorg. Chim. Acta* **1986**, *117*, 117–121.

(100) Kersting, M.; Friebel, C.; Dehnicke, K.; Krestel, M.; Allmann, R. Synthese, IR- und EPR-Spektren sowie die Kristallstruktur von $HPPh_3[WOCl_4(OPPh_3)]$. *Z. Anorg. Allg. Chem.* **1988**, *563*, 70–78.

(101) Voigt, A.; Abram, U.; Kirmse, R. The Existence of $[ReNF_4]^-$ - an EPR Study. *Inorg. Chem. Commun.* **1998**, *1*, 141-142.

(102) Voigt, A.; Abram, U.; Böttcher, R.; Richter, U.; Reinhold, J.; Kirmse, R. Q-Band Single-Crystal EPR Study and Molecular Orbital Calculations of $[(C_6H_5)_4As][Re^{VI}NCl_4/Re^{V}OCl_4]$. *Chem. Phys.* **2000**, *253*, 171–181.

(103) Lack, G. M.; Gibson, J. F. EPR in the $[ReNCl_4]^-$ Ion. *J. Mol. Struct.* **1978**, *46*, 299–306.

(104) Abram, U.; Voigt, A.; Kirmse, R. The Reaction of Rhenium Nitrido Complexes with CPh_3^+. Synthesis, Structures and EPR Spectra of Rhenium Imido Compounds. *Polyhedron* **2000**, *19*, 1741–1748.

(105) Abram, C.; Braun, M.; Abram, S.; Kirmse, R.; Voigt, A. $(NBu_4)[ReNCl_4]$: Facile Synthesis, Structure, Electron Paramagnetic Resonance Spectroscopy and Reactions. *J. Chem. Soc., Dalton Trans.* **1998**, 231-238.

(106) Voigt, A.; Abram, U.; Strauch, P.; Kirmse, R. An EPR Study of Tetra-*n*-butylammonium Tetrabromo-nitridorhenate(VI), $[(n\text{-}C_4H_9)_4N][ReNBr_4]$. *Inorg. Chim. Acta* **1998**, *271*, 199-202.

(107) Borisova, L. V.; Ermakov, A. N.; Plastinina, Y. I.; Prasolova, O. D.; Marov, I. N. Determination of Rhenium Based on the Formation of Rhenium(VI) Oxide Halide Complexes by Spectrophotometry and Electron Spin Resonance Spectroscopy. *Analyst* **1982**, *107*, 500–504.

(108) Holloway, J. H.; Hope, E. G.; Raynor, J. B.; Townson, P. T. Magnetic Resonance Studies on Osmium Pentafluoride Oxide. *J. Chem. Soc., Dalton Trans.* **1992**, 1131–1134.

(109) Holloway, J. H.; Raynor, J. B. Electron Spin Resonance and Raman Spectra of $[ReOF_5]$ and Related Species in Aqueous Hydrofluoric Acid. *J. Chem. Soc., Dalton Trans.* **1975**, 737–741.

(110) García, M. P.; Jiménez, M. V.; Oro, L. A.; Lahoz, F. J.; Alonso, P. J. A Paramagnetic, Mononuclear Organometallic Iridium(II) Complex: $[Ir(C_6Cl_5)_2(cod)]$. *Angew. Chem. Int. Ed.* **1992**, *31*, 1527–1529.

(111) Rivada-Wheelaghan, O.; Ortuño, M. A.; García-Garrido, S. E.; Díez, J.; Alonso, P. J.; Lledós, A.; Conejero, S. A Stable, Mononuclear, Cationic Pt(III) Complex Stabilised by Bulky N-Heterocyclic Carbenes. *Chem. Commun.* **2014**, *50*, 1299–1301.

(112) Alonso, P. J.; Alcalá, R.; Usón, R.; Forniés, J. EPR Study of Mononuclear Pt(III) Organometallic Complexes. *J. Phys. Chem. Solids* **1991**, *52*, 975–978.

(113) Hetterscheid, D. G. H.; Kaiser, J.; Reijerse, E.; Peters, T. P. J.; Thewissen, S.; Blok, A. N. J.; Smits, J. M. M.; de Gelder, R.; de Bruin, B. Ir^{II}(ethene): Metal or Carbon Radical? *J. Am. Chem. Soc.* **2005**, *127*, 1895–1905.

(114) Ionkin, A. S.; Marshall, W. J. Rare Organometallic Complex of Divalent, Four-Coordinate Iridium: Synthesis, Structural Characterization, and First Insights into Reactivity. *Organometallics* **2004**, *23*, 6031–6041.

(115) Meiners, J.; Scheibel, M. G.; Lemée-Cailleau, M.-H.; Mason, S. A.; Boeddinghaus, M. B.; Fässler, T. F.; Herdtweck, E.; Khusniyarov, M. M.; Schneider, S. Square-Planar Ir(II) and Ir(III) Amido Complexes Stabilized by a PNP Pincer Ligand. *Angew. Chem. Int. Ed.* **2011**, *50*, 8184–8187.

(116) Autschbach, J.; Zheng, S.; Schurko, R. W. Analysis of Electric Field Gradient Tensors at Quadrupolar Nuclei in Common Structural Motifs. *Concepts. Magn. Reson. Part A* **2010**, *36A*, 84−126.

TABLE OF CONTENTS GRAPHICS